8-2015

Enzyme Catalyzed Alginate Nanogels for Drug Delivery

Danna Nichole Sharp
University of Tennessee - Knoxville, dsharp9@vols.utk.edu

To the Graduate Council:

I am submitting herewith a thesis written by Danna Nichole Sharp entitled "Enzyme Catalyzed Alginate Nanogels for Drug Delivery." I have examined the final electronic copy of this thesis for form and content and recommend that it be accepted in partial fulfillment of the requirements for the degree of Master of Science, with a major in Chemistry.

Alexei P. Sokolov, Major Professor

We have read this thesis and recommend its acceptance:

S. Micheal Kilby II, Tessa R. Calhoun, Paul M. Dalhaimer

Accepted for the Council:
Carolyn R. Hodges

Vice Provost and Dean of the Graduate School

(Original signatures are on file with official student records.)

Enzyme Catalyzed Alginate Nanogels for Drug Delivery

A Thesis Presented for the

Master of Science

Degree

The University of Tennessee, Knoxville

Danna Nichole Sharp

August 2015

ACKNOWLEDGMENTS

I would like to thank my advisor Dr. Alexei Sokolov for all of his help and guidance in my research. Most substantially, I would like to thank Dr. Vera Bocharova for contributing so much to my graduate education by taking the time to help me understand concepts, ideas, instruments and literature in the field. Without her guidance this work would not be so commendable due to her important contributions. Additionally, I would like to thank Dr. Daisuke Sawada and Dr. Shiwang Chen for the measurements they performed for this work.

Furthermore I appreciate all of my colleagues in the Sokolov research group that have helped me throughout my graduate studies. I want to thank them for their friendship and guidance. Also without the support of my family and friends, I would not have come nearly so far. This work would not have been possible without the emotional support provided from my parents and Kevin Sinclair. It has been a blessing to have such steadfast people in my life.

ABSTRACT

Developing nanoscale carriers for the delivery of therapeutics is an important topic of investigation in current biomedical research. As opposed to traditional drug delivery systems, nanoscale systems offer enhanced tissue and cell permeation in addition to reducing drug elimination from the body. Biological based therapeutics such as DNA and proteins are now widely employed in medical applications and research has focused on using nanoscale drug delivery systems to administer these more effectively. Current synthesis methods of nanoscale biotherapeutic carriers face significant challenges. Among these are creating carriers with: sizes between 10-200 nm, low polydispersity, and non-cytotoxic materials. In this thesis, a nanocarrier synthesis method that meets these criteria is demonstrated using enzymatic methods to create monodisperse carriers that are 100 nm or less in size from entirely non-synthetic components. In the past, enzymatic synthesis of carriers has been limited due to the sensitivity and specificity of enzyme reactions to the presence of certain functional groups, substrates, temperatures, and pH's. In the following work, we use the enzyme laccase to serve as a catalyst for the growth of hydrogel nanoparticles. It is known that laccase has the ability to convert iron (II) cations to iron (III) cations. Additionally, the biologically derived polymer called alginate exhibits crosslinking in the presence of iron (III) to form an aqueous polymer gel matrix. Using these three components, alginate polymer, laccase enzyme, and iron (II) sulfate, nanoscale hydrogel carriers were synthesized. Furthermore, we found that the size and polydispersity of the particles could be controlled through limitation of the enzyme activity. Dynamic light scattering, UV-Visible spectroscopy, Small Angle Neutron Scattering, and Atomic force microscopy were used to characterize the particle's size, dispersity, growth rate, and growth mechanism. Using 0.36 mM iron (II) sulfate, monodisperse particles with a radius of 40 nm were formed. Increasing iron concentration increased the size and speed of the formation of the particles which resulted in their aggregation after reaching 100 nm in size. Here we have achieved simple synthesis of biodegradable nanogel particles with a hydrodynamic radius of 100 nm and below whose size can be tuned and exhibits low polydispersity.

TABLE OF CONTENTS

Pages

Chapter 1: Introduction……...1

1-1 Current Directions in Drug Delivery Systems……1

1-2 Current Nanoscale Delivery Systems…….5

1-3 Nanogel Synthesis, Current Techniques and Materials……10

1-4 Hydrogel Nanoscaling Techniques……...14

Chapter 2: Synthesis and Characterization Techniques……....19

2-1 Synthesis of Nanogel Particles……..19

2-2 Characterization with UV-Visible Spectroscopy…….....22

2-3 Characterization with Dynamic Light Scattering…….23

2-4 Characterization with Atomic Force Microscopy…….28

2-5 Characterization with Small Angle Neutron Scattering……...….30

2-6 Characterization with Viscometry and Rheology…….37

Chapter 3: Results……41

3-1 Enzymatic Induced Gelation……41

3-1-1 Enzyme Kinetics…..……41

3-1-2 Polymer Molecular Weight..…….44

3-1-3 Gelation……44

3-2 Enzymatic Production of Nanogel Particles……46

3-2-1 Dynamic Light Scattering…….....46

3-2-2 Atomic Force Microscopy ……...49

3-2-3 Small Angle Neutron Scattering……52

Chapter 4: Discussion……...57

4-1 Mechanism of Nanogel Growth……..……..57

4-2 Tuning Nanogel Particles……..…..……..60

4-3 Assessment of Drug Delivery Capability……..64

Chapter 5: Conclusion……...65

References……67

Vita……76

LIST OF FIGURES

Figure 1-1. Effect of size on uptake of poly(ethylene imine) (PEI) coated gold nanoparticles into mammalian cells……..2

Figure 1-2. Several types of popular drug delivery particles……...9

Figure 1-3. An example of chemical crosslinking to form nanogels with a click synthesis method published by Heller et al……11

Figure 1-4. Physical crosslinking via ion-polymer charge condensation……..14

Figure 1-5. Particle Replication In Nonwetting Templates (PRINT)……16

Figure 1-6. Microfluidic synthesis of charge condensated nanogels……17

Figure 2-1. Ionically crosslinked "egg box" structure of alginate with specific hard cations…...19

Figure 2-2. Reaction of the laccase enzyme catalyst……20

Figure 2-3. Absorption of energy via excitation of a molecule with light……22

Figure 2-4. Schematic of UV-Vis instrument……23

Figure 2-5. Schematic of the DLS set up used……...24

Figure 2-6. Example of how the correlation of intensity data is plotted versus lag time to obtain correlation functions……..26

Figure 2-7. Example of how a stretched correlation function is formed……...28

Figure 2-8. Example of the common scanning modes of AFM……....29

Figure 2-9. A schematic presentation of a typical neutron scattering experiment. As d_s increases, θ decreases, and thus q decreases as well……...……...31

Figure 2-10. How scattering length fluctuates as neutrons interact with different parts of the solution. ……33

Figure 2-11. An example of how the form factor P(q) changes with q for cylindrical particles...36

Figure 2-12. Example of a creep experiment……39

Figure 3-1. Absorbance of iron (III) acetate complex at 400 nm, pH 6.0……42

Figure 3-2. Graph (A) shows the concentration of iron (II) calculated from the absorbance of the iron (II) 1-10 phenanthroline complex at 508 nm.……43

Figure 3-3. Viscosity data plotted versus concentration, c, to estimate the intrinsic viscosity [η]……..45

Figure 3-4. Demonstration of bulk gelation.....45

Figure 3-5. Films synthesized with 0.67 wt% alginate, 0.03 mg/ml (0.44 U/ml) enzyme and iron (II)……....45

Figure 3-6. Change in the normalized intensity correlation functions of (A) 0.36mM iron and (B) 3.6 mM iron over time……..48

Figure 3-7. The three types of correlation functions observed throughout nanogel growth…….48

Figure 3-8. ((A) Change in the hydrodynamic radius and stretching parameter, β, (polydispersity) of the particles over time when synthesized with 0.36 mM iron and (B) with 3.6 mM iron. The three regions are marked as I, II, and III……..49

Figure 3-9. Tip broadening of A). a tip with no width(ideal), and B). a tip with width (real)…..50

Figure 3-10. AFM images and size distributions of nanogel particles diluted 50 times from their original solutions……..51

Figure 3-11. (A) shows the nanogel particles after 60 min of reaction with 3.6 mM iron. B) is a control with only laccase (0.187 U/ml), and C) a control containing laccase (0.187 U/ml) and alginate (0.07 wt%) but no iron……51

Figure 3-12. SANS spectra of alginate gel in solvents: (a) H_2O and (b) D_2O as a function of Fe^{2+} ion concentration ranging from 1.5 to 45 mM……..55

Figure 3-13. Unified model fitting. Blue lines represent the Guinier fit and green the Porod…..56

Figure 4-1. Proposed mechanism of nanogel particle growth……...59

CHAPTER 1: INTRODUCTION

1-1). Current Directions in Drug Delivery Systems.

Development of drug delivery systems for medical applications is an important topic of research in today's society. They are used in drug delivery to enhance the efficacy of administered therapeutics in the body. These delivery devices impart desirable characteristics to drugs such as extended release time[1], specific tissue targeting[2], stimulus induced release[3], altered solubility[4], and more. Furthermore, drug carriers allow the delivery of sensitive therapeutics, such as biomolecules, inside the body because they easily degrade quickly when freely administered to patients. However, most developed synthesis methods for biomolecule carriers contain certain manufacturing hurdles. The aim of this research is to construct and characterize an improved method for the synthesis of nanoscale drug carriers to contain biological therapeutics such as proteins, DNA, RNA, and enzymes. In order to understand the synthesis considerations and rational behind any design scheme, it is important to describe the limitations in current research and what makes a successful drug carrier.

When designing an efficient drug carrier, there are certain aims that improve the efficacy of delivery devices. The first aim is to limit the size of the carrier so that it is between 10 and 200 nanometers. Particles smaller than 10 nm are known to be rapidly cleared from the body via the renal system.[5] However, particles larger than 200 nm have a greatly reduced efficiency at entering the cytosol of cells.[6] Delivery vesicles in this size range typically exhibit desirable properties such as increased tissue/cell penetration, evasion of the immune system, and targeting to drug delivery sites.[7,2] All of these characteristics allow higher percentages of intact therapeutics to reach the specific sites in the body upon which they enact to more effectively alter the health of the patient (Figure 1-1).

Additionally, controlling the size of particles allows drugs to be used to target specific tissues in the body. Many authors have shown that particles of a certain size are selectively internalized by tumor tissues.[2,8] For example, in a paper by Zhang et al., gold nanoparticles coated with polyethylene glycol of diameter of 20 nm showed higher uptake by tumor tissues than particles of 40 nm and 80 nm in size.[9] Such targeting technology will improve future drug efficacy in patients and allow administration of lower amounts of therapeutic as smaller doses are more effective due to targeting technology.

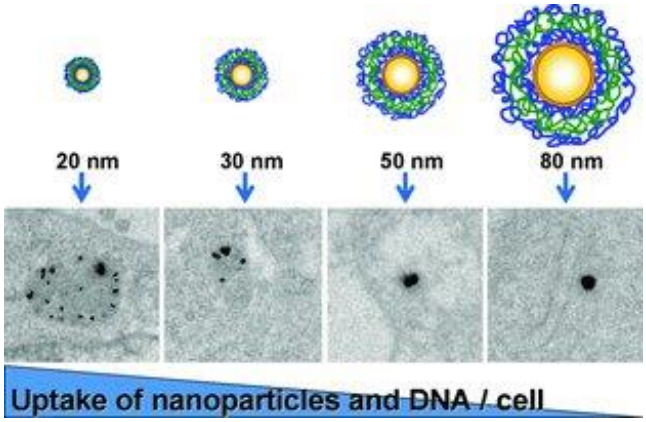

Figure (1-1). Effect of size on uptake of poly(ethylene imine) (PEI) coated gold nanoparticles into ovarian CHO-K1 cells.[10]

The uptake of drug particles into the cytosol of cells is thought to occur via endocytosis. This is a process that cells utilize to internalize substances that cannot pass through their semipermeable lipid membrane. Endocytosis occurs when the cell membrane wraps itself around the particle on the surface to enclose it within the membrane. This enclosed particle is pulled inward so that it is broken off from the membrane and drawn inside the cell where it is directed to an appropriate organelle.[11] There are multiple types of endocyctosis that can be used to internalize particles: phagocytosis, caveolae-mediated endocytosis, macropinocytosis, and clathrin- and caveolae-independent endocytosis.[12] Most articles do not delve into the specific type of endocytosis used to internalize particles since the process varies greatly depending on the size, identity, and other properties of the particles. Although the method through which drug particles are internalized is not consistent, experimental evidence is plentiful in regards to the effect of particle size on cell internalization. It is well known that the ideal particle size for cell entry lies between 10 and 200 nanometers for most cell types. Therefore, aiming to create a carrier of this size is ideal for optimal delivery of therapeutics inside cells of the body.

Besides the optimization of size for the improvement of nanocarrier efficiency, there are other properties that are beneficial for biological therapeutic delivery systems to exhibit. These include: low particle size dispersity, water solubility, synthesis without the use of harsh solvents, and slow drug release profiles.

Low Particle Size Dispersity. When limiting the size of drug carriers to below 200 nm during synthesis, the problematic issue of high particle dispersity usually appears.[13,14] This occurs at the nanoscale because growth is usually much harder to control as experimental parameters become more rigid. Therefore, minute variations in the experimental conditions will produce large changes in the resulting particle's characteristics.[15] This association causes problems in many synthesis methods where either size or polydispersity is well controlled, but not both.[16,17,18] It is desirable that drug carriers are synthesized with both homogenous size and low particle size dispersity because it ensures that delivery of the drug cargo is uniform from all particles.[19] If all carriers are of the proper size to enter cells, then there is a higher probability that the carriers deliver drugs more efficiently. Additionally, uniform particle sizes will ensure that the liberation of therapeutics from each carrier follows the same release pattern.[19] The diffusion of particles through the carrier matrix and into the body will occur on the same time scale if particles are uniform. This allows physicians to more accurately predict the lifetime of an encapsulated drug in the body and increases safety of the developed therapeutic for clinical use.

Water Solubility. Hydrophilic composition of drug carriers has traditionally been viewed as undesirable for drug delivery since hydrophobic particles have extended release/breakdown times in the body. This property gives some insoluble drugs twice the lifetime of that of soluble therapeutics.[20] However, water soluble carriers offer the advantage of decreased aggregation, higher cell permeability[21], and non-toxic environments for the encapsulation of biological therapeutics.[22] In fact, many hydrophobic drugs must be altered with the addition of hydrophilic moieties to prevent their toxicity in vivo.[23] Hydrophilic properties allow carriers to remain more uniformly distributed in solution, to avoid toxicity due to particle aggregation within cells, and to degrade less of the encapsulated therapeutic.[23] Furthermore, aqueous environments within the carriers will stabilize biological molecules such as DNA and proteins that are frequently used in biomedicine applications. All of these factors indicate that purely hydrophilic or hydrophobic drug carriers are not ideal and that an appropriate mixture of both properties will impart the best drug efficacy with minimal damage to biological components.

Synthesis without Harsh Solvents. Many methods by which nanoparticle drug carriers are made involve the use of harsh chemicals or synthesis conditions. Examples of these methods include: the use of radiation to initiate polymerization[24], organic solvents[25], and radical chemistry[26]. Minimizing the use of denaturing components allows for the encapsulation of biological therapeutics such as proteins, DNA, RNA, and enzymes. Typically, carriers designed to contain biological materials must be extensively purified before loading the drug to remove denaturing contaminants.[27] This complicates and extends the synthesis time of carriers. Development of a water-based synthesis method for nanoparticle production is one way to avoid such contamination to ensure effective and simple bio-therapeutic encapsulation. An example of this was demonstrated by Wang et al. where a copolymer carrier was synthesized in water using self-assembly techniques to encapsulate DNA with high efficiency. They also did not require a purification step before loading the particles with therapeutic.[28]

Slow Drug Release Profile. When drugs are delivered into the body, the rate and duration at which they are released is an important parameter of clinical concern. By slowing down the release of a drug, the time over which it remains active in the body is extended.[29] This helps maintain consistent therapeutic levels in the blood and increases patient compliance as administration is less frequent. During carrier design, the functional groups on the exterior of the particle can be altered to slow down drug liberation. Functional group hydrophobicity, charge, and identity can all drug release profiles.[30] For example, Akala et al. developed a copolymer that only degrades when the solution pH changes from acidic to neutral. The real life application of such a carrier system is to protect the therapeutic from degradation in the stomach and invoke release in the intestinal tract once pH returns to neutral.[31] Other examples include: constructing carriers with an affinity for the drug molecule in order to slow release[32], mixing slowly degrading polymers into the carrier matrix to increase mechanical strength[33], and coating the exterior of particles with a slowly degrading material[34].

1-2). Current Nanoscale Drug Delivery Systems.

Among the nanoscale drug carrier systems that meet the size requirements for optimum delivery (between 10-200 nm), several types of materials and encapsulation strategies exist. The most well-known of these are: nanoparticle/nanocapsules, polymer-drug conjugates, liposomes, polymers/block copolymers, self-assembled systems, and nanogels.[35] These systems are all outlined in Figure 1-2. This thesis however will focus only on the synthesis of nanogels and their optimization as drug carriers. Nanogels offer good biocompatibility with biological molecules due to their high water content and non-toxic synthesis and breakdown. Most other nanoscale carriers currently used in drug delivery applications are challenged in these aspects and/or have complex synthesis methods.

Metal-based Nanoparticles and Organic Frameworks. Nanoscale carriers that are primarily composed of metallic components can be categorized into two types: nanoparticles and metal-organic frameworks (MOFs). Beyond the inclusion of metals in their structure, these carriers are very different. Metallic nanoparticles are simply nano-sized particles of metallic components. Their synthesis is well established and most particles can be made with controlled size, shape, and polydispersity.[36] Drug delivery via nanoparticles typically occurs by attachment or adsorption of the therapeutic onto the exterior of the particle. For example, Brown et al. designed a gold nanoparticle drug carrier on which they tethered the anticancer drug oxaliplatin for delivery into tumor cells.[37] Another synthesis by Bhumkar et al. was performed by reducing a gold solution with the biodegradable polymer chitosan to form gold nanoparticles coated with the polymer. The authors demonstrated loading of insulin onto the polymer coating via simple incubation. The polydispersity of the carriers was too wide as their size typically varied from 10-40 nm, however delivery efficiency of insulin in vivo for mice was significantly improved using the particles.[38]

Another type of metallic-based nano carrier called nanoMOFs are nanoscale frameworks composed of both organic and metal components. Whereas nanoparticles can only attach drugs to their surfaces, nanoMOFs can encapsulate drugs and due to their high porosity which allows considerable drug loading in their matrices.[39] An example of drug encapsulation can be seen in a paper by He et al. where UiO-nanoMOFs (based on a zirconium oxygen species with

dicarboxylate linkages) were loaded with siRNA. NanoMOF particles had a low polydispersity and diameter of approximately 100 nm. A high loading efficiency of siRNA biotherapeutic was shown to occur by heavy adsorption of the ribonucleotide to the exterior of the particle.[40] Unlike nanoparticles, nanoscale MOFs are a new technology and the optimization of size and polydispersity has not yet been extensively explored.[39] Overall metallic nanoparticles and nanoMOFs can offer one or more valuable drug delivery properties such as well-defined size, low polydispersity, and high loading capacities. In vivo toxicity of nanoMOFs has been reported to be low in two studies[41,42], but further safety investigations must be undertaken before such therapeutic carriers become widely used. Additionally, the safety of many metallic nanoparticles in vivo has been shown to be questionable in scientific literature.[43 Jeng]

Polymer-Drug Conjugates. Polymer-drug conjugates are single polymer chains that have been covalently bonded to the therapeutic molecules themselves. Using polymers instead of nanoparticles is beneficial because the toxicity and biocompatibility of most polymers are known. In addition, there are quite a few naturally derived polymers available for synthesis that decompose into non-toxic derivatives. Polymer conjugates are very small since they are usually only composed of one polymer chain and one drug molecule.[44] An example of a conjugate can be seen in a paper by Bailon et al. where they accomplished PEGylation of interferon protein. They initiated conjugation via pH adjustment of a succinimidyl functionalized PEG and purified the product multiple times on a column and then concentrated the product. They showed that enzyme activity was decreased to 7% from the initial protein, however the drug had an increase in efficacy in vivo which they explained was due to an increase in retention time.[45] Their technology has been patented under the name PEGasys and is now used to treat patients with hepatitis C. Although no issues with this conjugate have arisen, other conjugate based carriers frequently exhibit issues such as immunogenicity.[46] Additionally, the polydispersity of polymer drug conjugates is difficult to reduce since it is dependent on many factors such as the purity of the utilized polymer, number of polymers attached to the drug, the site of attachment, and purity of the isolated conjugate. Another consideration during synthesis is that conjugation of drugs typically attenuates or enhances their elimination in vivo. Therefore, many design schemes incorporate release mechanisms into the drug-polymer linkage.[47] Despite these setbacks, new site specific attachment schemes that include activated release mechanisms are in development,

however many still require complex synthesis and purification steps due to the demands required for an efficient conjugate carrier.[46]

Liposomes. Liposomes make excellent biocompatible and biodegradable drug carriers. They are composed of a self-assembled bilayer of lipids within which a hydrophilic drug resides in an aqueous environment. The lipid exterior of these particles is useful in drug delivery because it interacts with the lipid bilayer membrane of cells. This assists with uptake of the drug payload and its penetration into the cell cytosol.[48] Synthesis of these carriers is usually achieved by simple micro-emulsion techniques.[49] However, when trying to synthesize liposomes below 100 nm, the process quickly becomes challenging and polydispersity of the resulting particles is usually very high.[50] In addition, the mechanical strength of liposomes is low so that in vivo they release their drug payloads very quickly as they degrade. Therefore liposomes are hard to use for extended release applications unless they are chemically modified.[51]

Polymers/block copolymers. Polymers and block copolymers are useful materials in the synthesis of nanoscale drug carriers. One benefit they offer is a plethora of different types of molecules to choose from which allows for a broad range of properties to be instilled in carriers in addition to biocompatibility. For example, polymers can selectively degrade or unfold based on the presence of a specific pH, temperature, solvent, pressure, etc.[31] The degree of response of these molecules can also be finely tuned during synthesis by changing the functional groups on the molecules or chemically attaching different polymers together to form block co-polymers. Because of these widely variable properties, the encapsulation and control of drug release from polymer based carriers is quite refined. The main challenge when synthesizing polymer drug carriers is the synthesis of nanosized particles below 100 nm. Typically, radical polymerization is used to synthesize small polymer particles.[52] However, this is carried out in very harsh environments with toxic solvents and reactive molecules. In order to make a biocompatible carrier that is safe for in vivo use, the resulting product must be extensively purified which can be a time intensive process. Additionally, polydispersity of nanosized polymer particles is difficult to control by traditional means. Specific techniques are usually employed to achieve monodisperse nanosized polymer particles. However, these techniques still have limitations that may reduce their efficiency or feasibility as drug carriers in biomedicine.[52]

Self-Assembled Systems. Self-assembled drug carriers consist of carrier molecules that form particles through innate attraction of carrier components. Typical building blocks include charged polymers[53] and proteins[54,55] which impart biocompatible and biodegradable properties to the carriers. The advantages of these types of systems are due to the very monodisperse and small sizes that arise from this technique. For instance, nanocarrier particles consisting of self-assembled β-Lactoglobulin protein near 60 nm have been reported with low polydispersity values.[56] However, synthesis methods usually cannot be tailored to give another particle size since the self-assembly process is not easily altered.[57] In order to make carriers of a different size, it is typically required that an entirely new polymer or protein of a different identity or size is used.

Nanogels. Nanogels are useful biological drug carriers composed of nanosized hydrogels. They will be the drug carrier of focus in this thesis due to their biocompatibility and simple synthesis. These carriers are made out of cross-linked polymers and have a very high water affinity. This allows them to swell in aqueous environments to accommodate or release therapeutics. Similar to other polymer based systems, nanogels are frequently made with biocompatible and biodegradable materials. Furthermore, the high water content in their matrixes creates a favorable environment for the encapsulation and stabilization of biological therapeutics.[58] They are additionally useful because the degree of crosslinking in the polymer matrix can easily be manipulated which allows for precise control over porosity of the synthesized hydrogel drug carriers.[59] Control over this parameter helps retard and control the release rate of therapeutics from the nanogels. Due to these favorable characteristics, nanogels will be the encapsulation material of focus in this thesis. Encapsulation of biological materials is best accomplished when activity and structure of the materials are preserved and protected until they reach their desired target in the body. Nanogels are a platform that offer this in a simple and effective manner.

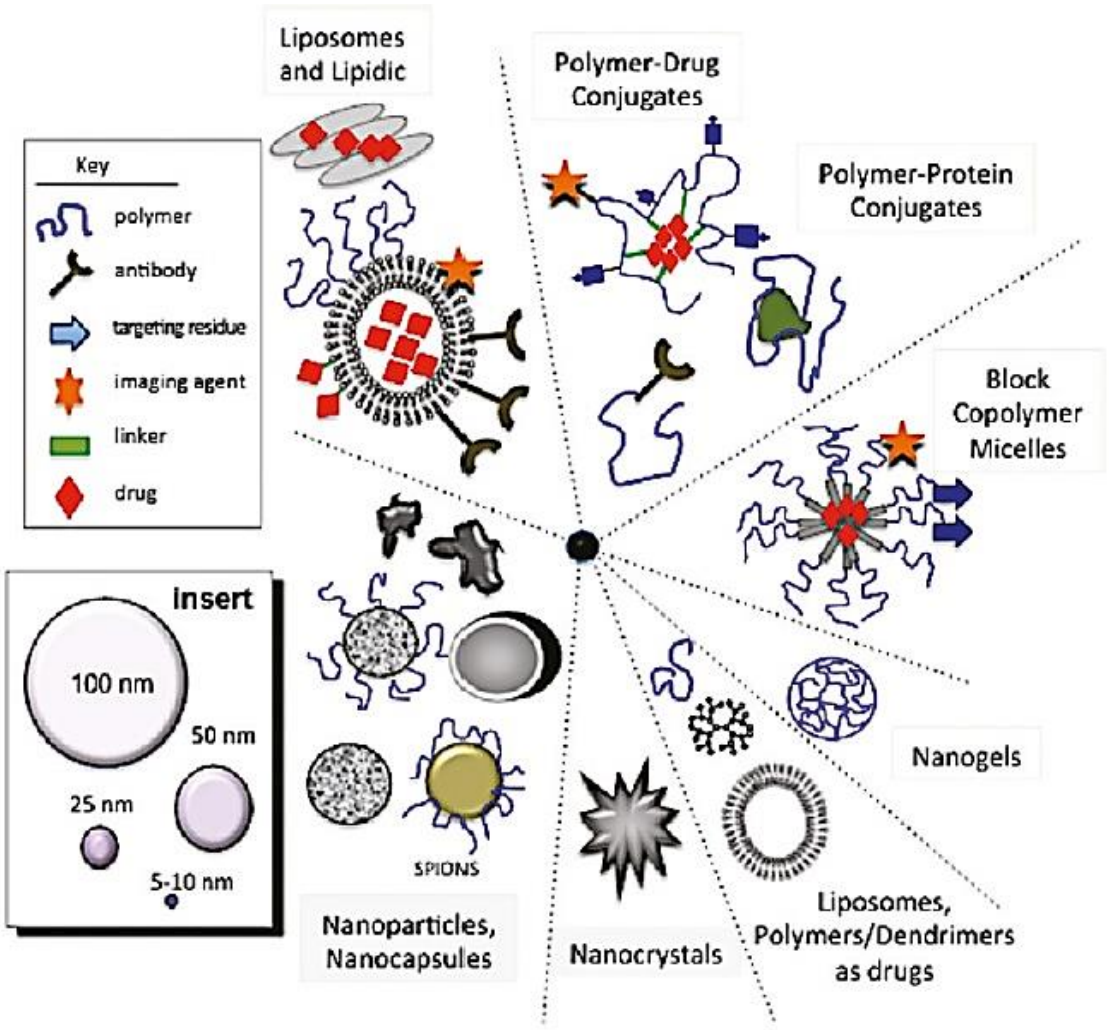

Figure (1-2). Several types of popular drug delivery particles. Self-assembled particles are not shown.[36]

1-3). Nanogel Synthesis, Current Techniques and Materials.

Biocompatible nanogels and hydrogels can be synthesized with three primary techniques. This is by the use of chemical, physical, and enzymatic crosslinking methods. Chemically cross-linked gels offer the advantage of stronger mechanical strength. This prevents their degradation in vivo and extends drug release time. However, when focusing on the encapsulation of biological therapeutics, chemical crosslinking is difficult to use without lengthy purifications steps due to the denaturing and harsh synthesis conditions. Physically cross-linked gels and enzymatic gels are useful in this regard because they are both biocompatible and biodegradable even though their mechanical strength is lower.[60] Enzymatic crosslinking is furthermore unique because it can substitute for either chemical or physical crosslinking and does not involve the use of cytotoxic reactants. However, this method has not been widely used due to the specificity of enzymes to their substrates and their sensitivity to environmental conditions.

Chemical Crosslinking. The polymers in chemically crosslinked gels are cross-linked using chemical means to form a covalent bond between the matrix components.[52] There are many methods by which this is typically accomplished. One is by regular radical polymerization. In a study by Edman et al., a hydrogel was made from dextran polymers cross-linked with bisacrylamide using emulsion polymerization in a mixture of chloroform and toluene. Although dextran is a biocompatible polymer, the resulting hydrogel had to be extensively purified before application to remove all of the remaining excess bisacrylamide, chloroform, and toluene in order to be considered biocompatible.[61] Another type of chemical crosslinking can be achieved by exposure to radiation. This can be done using either heat or light as an initiator. Raemdonck et al. used this method to produce nanogels via inverse miniemulsion photopolymerization. They used a mixture of biocompatible dextran monomers, methacrylate monomers, and photoinitiator to create the nanogel matrix upon exposure to 365 nm wavelength light. Again, these gels had to be put through an intensive purification process in order to be used for siRNA loading.[62] Another method by which nanogels are made is through click chemistry. Known for its ability to perform chemical reactions in aqueous environments, click chemistry is a good method to crosslink polymers to form biocompatible hydrogel drug carriers. An example of a click nanogel synthesis can be seen from Heller et al. (Figure 1-3) where they used biphosphate-functionalized dextran

cross-linked by copper alkyne-azide cycloaddition.[63] Although a simple synthesis, in order to remove the copper contamination a multiple day purification protocol had to be followed. There are other types of click chemistry that are used to synthesize nanogels, however nearly all have contaminants, complex synthesis, or unfavorable side reactions with which to contend.[64]

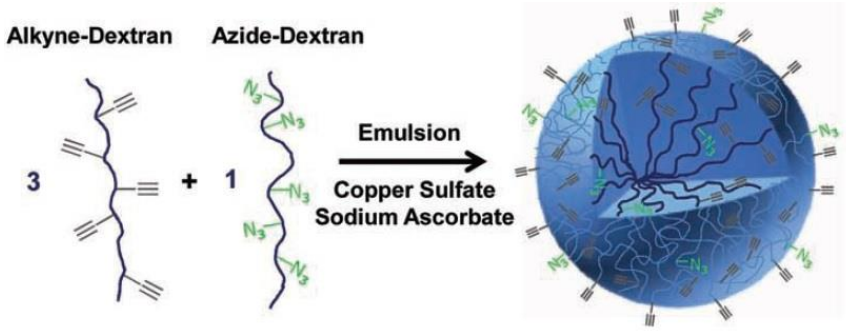

Figure (1-3). An example of chemical crosslinking to form nanogels with a click synthesis method published by Heller et al.[63]

Physical Crosslinking. When aiming for the encapsulation of biological therapeutics, a much more biocompatible choice is the use of physically cross-linked nanogels. These are created when polymers are cross-linked in a manner that is not covalent.[52] Although the linkages are less sturdy and therefore degrade more quickly, physically cross-linked gels are very simple to make and typically require no purification steps before use. Additionally, synthesis can occur at room temperature, physiological pH, and in aqueous solution. Some attractive forces used to crosslink nanogels include hydrogen bonding, hydrophobic aggregation, stereocomplexation, and charge condensation.[59] Gels physically crosslinked through hydrogen bonds demonstrate problems when used for delivery applications as the bonds are so weak that the gels dissolve in a matter of hours.[59] Hydrophobically aggregated gels are usually not appropriate for biotherapeutic delivery as the interior environment of the gel is hydrophobic which disrupts the organization of many biological molecules.[65] Stereocomplexation, which refers to the attraction between enantiomers, is also suboptimal due to the sensitivity of the complexed bonds to polymer identities and the dominant solvent.[59] There are other types of reversible interactions that can be used to make gels, however,

they are not extensively used in literature and will thus not be discussed. For in vivo drug delivery purposes, charge condensation is a good biocompatible and simple option.

Charge condensation is the simplest method of the listed physical crosslinking methods and thus the most widely used. Charge condensation occurs in solution when two oppositely charged molecules exhibit a strong enough attraction for each other to create a cross-linked matrix. This gelation process can occur between many types of molecules such as: polymers with opposite charges and polymers and ions with opposite charges (Figure 1-4).[59] The novelty of synthesizing hydrogels with charge condensation comes from the simplicity of the synthesis method which usually only requires 2-3 steps and does not need any final purification before use. An example of a nanogel synthesized using this method comes from authors Papadimitriou et al. They used chitosan grafted poly(ethylene glycol) copolymers cross-linked with both poly(glutamic acid) and tripolyphosphate to encapsulate bovine serum albumin (BSA) protein and slow its release. They demonstrated an increase in the time at which 80% BSA is released from an initial 20 hours to 80 hours in vitro with their system.[66]

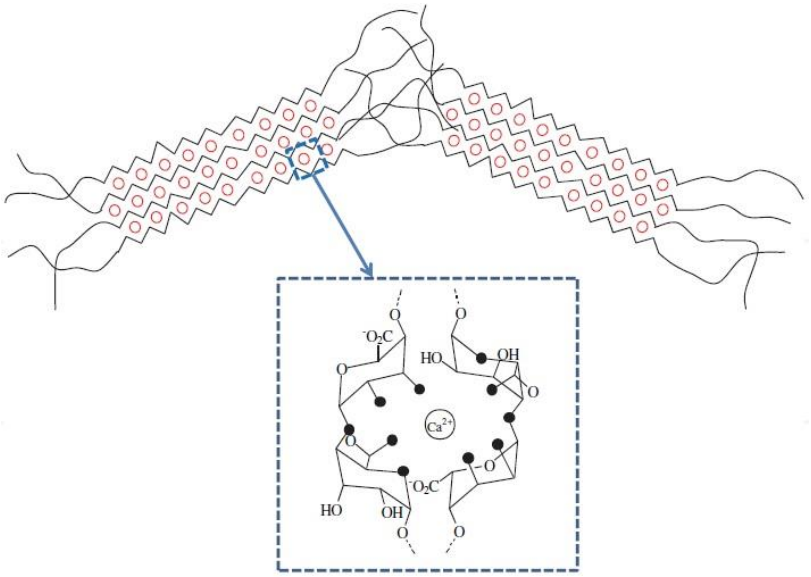

Figure (1-4). Physical crosslinking via ion-polymer charge condensation. Here calcium ions attract the negative oxygen atoms (black dots) on the polymer chain.[67]

Enzymatic Crosslinking. Currently this method is not widely used, however enzymatic crosslinking is a good way to link polymers for the creation of biological drug carriers. Enzymes can be used to both chemically and physically crosslink hydrogel components. They serve as biocompatible catalysts that work to activate specific groups on the molecules in the solution.[68] Several examples of bulk hydrogel formation systems are listed in a review paper by Teixeira et al. Some notable strategies include: crosslinking of casein with microbial transglutaminase for extended release of Vitamin B12,[69] using Thermolysin enzyme to trigger reverse hydrolysis to crosslink proteins and *N*-(fluorenylmethoxycarbonyl),[70] and hydrogel formation via crosslinking of poly(ethylene glycol) functionalized with specific domains that crosslink upon exposure to transglutaminase enzyme factor XIIIa for encapsulation/stabilization of mammalian cells.[71] Due to the sensitivity of enzymes to environmental conditions that may inactivate them, such as hydrophobic solvents, pH, and temperature, enzyme catalyzed formation of nanogels has not yet been achieved to the best of our knowledge. This thesis will focus on the use of enzyme initiated crosslinking for the formation of nanogel drug delivery carriers. The system studied herein will show how these formerly limiting environmental parameters can be appropriately adjusted to regulate nanogel particle size and dispersity.

Nanogel Materials. There are many polymers that exhibit swelling in water and thus there are many materials from which nanogels can be synthesized. When developing a system for biological therapeutics, it is important that the carrier material be both biocompatible and biodegradable. Biocompatible materials are known to be neutral in regards to invoking cell death and are typically tested for disruption of cell, enzyme, and other biological processes. These are plentiful and are already widely used in current drug formulations. Biodegradable materials are less commonly used but still plentiful in literature. These are defined as materials that are able to degrade in common biological conditions. Some examples include polymers such as poly(lactic acid), poly(lactic-co-glycolic) acid, poly-ε-caprolactone, poly-alkyl-acyanoacrylate.[72] Furthermore, there are also polymers that are derived from biological sources in addition to being biocompatible and biodegradable. These non-synthetic polysaccharides are isolated from natural products and purified for industrial use.[73] Some examples include hyaluronic acid (derived from animals), chitosan (from insects), dextran (from bacteria), and alginate (from seaweed).[74] Of these, chitosan and alginate are unique because they will ionically crosslink upon exposure to certain

metal cations resulting in a very simple synthesis protocol.[75] This thesis will focus on the use of alginate for the development of nanogel drug delivery carriers instead of chitosan due to its ability to crosslink with the specific cations used in our synthesis scheme.

1-4). Hydrogel Nanoscaling Techniques.

Hydrogels are old technology and their synthesis has been known since the early 1960's.[76] However, nanogels are a more recent development, and their formulation has challenged researchers to find new routes through which to create such small hydrogel particles with low polydispersity for biological therapeutic encapsulation. In this thesis, the focus will revolve around nanogels created with an ionically crosslinked polymer and metal cation system. Typical synthesis methods through which these types of nanoscale biological therapeutic carriers are made include: microemulsion, nanomolding, microfluidics, and self-assembly.

Microemulsion. Microemulsion systems work by using two solvent phases, one hydrophilic and the other hydrophobic, to create micro or nanogels. The solution is mechanically perturbed by some force such as stirring or sonication to break up the phases and create small aqueous bubbles in the hydrophobic solvent. This method is designed so that the gel polymers are soluble only in the aqueous phase and thus crosslinking of polymers only occurs within the aqueous bubbles. An example from literature can be seen in a paper published by Nesamony et al. in 2012. In this synthesis, alginate was ionically crosslinked with calcium chloride in a mixture of water and an oil called isopropyl myristate. Upon sonicating, particles with a mean diameter of 6.7 nm with a large size distribution were formed.[77] However, in order to form such small particles, the use of a surfactant was required. Surfactants are typically used in microemulsion synthesis techniques but must be removed before drug loading, which introduces a purification step. Although the synthesis used by Nesamony et al. was very simple and quick, purification was still necessary and the size distribution of the resulting particles sub-optimal for good drug delivery devices.

Nanomolding. Nanomolding is a technique that uses a template formed with photolithography technology to create gels of uniform size and shape. Polymer solution is laid on an adhesive layer and non-wetting molds pressed into the solution. Afterwards polymerization is initiated by various means and the mold withdrawn so that the particles remain on the adhesive. The sticky layer is then dissolved with solvent to free the particles and afterwards they are purified back into aqueous solution (Figure 1-5).[78] This technique is quite complex to implement, but it offers the advantage of producing very precisely shaped and sized nanoparticles in large quantities. In a paper by Rolland et al. the synthesis of monodisperse 200 nm trapezoidal shaped nanogels made of poly(ethylene glycol) was demonstrated using photopolymerization and nanomolding techniques for the encapsulation of fluorescent avidin proteins. Confirmation of protein activity with confocal microscopy was accomplished via the submersion of the particles in a fluorescently labeled biotin solution. It was shown that encapsulation during the molding process did not alter the function of avidin since colocalization of the two fluorescence signals occurred.[78]

Another paper by Garcia et al. demonstrated the encapsulation of DNase was in nanomolded particles.[79] However, retention of biomolecule activity was not well documented. The authors only characterized activity by measuring size and conversion of methylene green in tris buffer solution. These tests may not have been sufficient enough to determine activity since it is known that the activity of DNase is negligible in solutions without calcium which was missing in their assays.[80] Meaning that when the authors saw no difference in between encapsulated and free DNase, it might have been due to lack of activity to begin with. The biocompatibility of this technique still requires further investigation as most photopolymerization conditions are harsh to biomolecules unless the light intensity, irradiation time, temperature, and organic solvent levels are tightly controlled.[81]

Figure (1-5). Particle Replication In Nonwetting Templates (PRINT). Nanomolding technique designed by Rolland et al.[78]

Microfluidics. Microfluidics was first developed as a technique to quantify small particles such as DNA and RNA.[82] The devices are made via soft lithography of polymers such as poly(dimethylsulfoxane) and polyurethane. However, the usefulness of the micro scale fluidic channel devices has expanded their use into many areas of research. Nanogel synthesis with microfluidic channels has been demonstrated and is now frequently used in literature.[83,84,85] Control over nanogel size and dispersity can be accomplished by manipulation of parameters such as flow rate and solution pH. For example H. Zhang et al. demonstrated the synthesis of monodisperse alginate nanogels of diameter 70 nm. They achieved size control by adjusting the flow rate of both the aqueous and non-aqueous phase (Figure 1-6).[86] This is one of the first systems used for the physical crosslinking of nanogels with the flexibility in synthesis to easily make nanogels of different sizes. They showed that multiple particle sizes can be made monodispersely without using different reactants or templates. Unfortunately, microfluidic devices are expensive to make and their output is very slow since their microsized channels can only pass one particle at a time.[87] Although it is a good laboratory method to produce nanogels for biotherapeutic drug encapsulation, manufacturing carriers with this technique on any scale for medical applications might encounter problems in production costs and output.

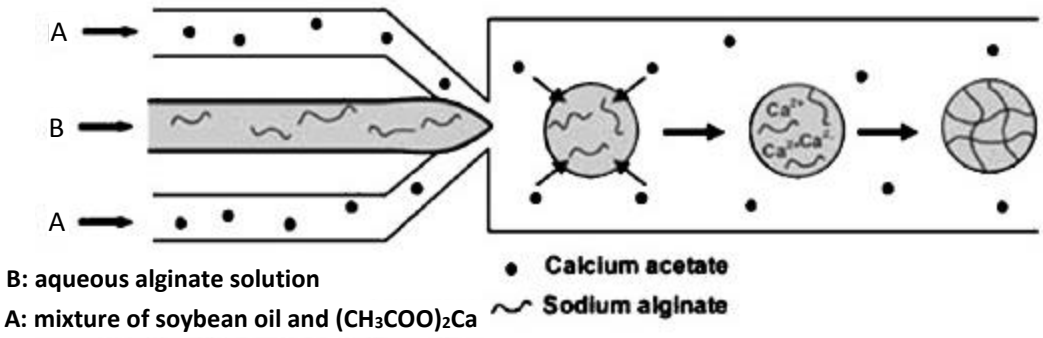

Figure (1-6). Microfluidic synthesis of charge condensated nanogels. Channel A contains the calcium ion crosslinker in oil and channel B contains alginate polymer in water.[86]

Self-assembly. The name of the self-assembly method explains itself. This technique uses components that have strong attractions to each other to self-assemble themselves into gel particles in aqueous solution. The two most common types of materials used in these systems are polymers and proteins. Some examples of nanogel components used for self-assembly include: wheat glutenin, thiolated heparin, biological copolymers, cholesteryl pullulan, and whey protein.[88,89,57,90,91] Sizes of the resulting particles ranged from 40 – 200 nm and particle distributions were typically difficult to control or not reported. Synthesis of self-assembled particles is useful because it is very simple, fast, and does not require a purification step. However, the drawback to self-assembled particles is that there is a lack of flexibility in regards to size differentiation. Making particles of different sizes with self-assembly methods typically requires the use of new starting materials. In order to make a polymer carrier with a different size, a new polymer of a different molecular weight must be first synthesized. For protein particles, this presents even more of a challenge since they cannot be modified as easily. In these scenarios it is usually easier to just find another protein with a different identity instead of attempting modification. This issue results from the lack of control over the particle growth method. Since the driving force for the particle formation is not regulated by the experimentalist but is dictated by the strength of the attraction between the used materials, resulting particle size cannot be changed during growth and must be altered beforehand.[57]

Table (1-1). A summary of current nanogel synthesis methods including benefits and drawbacks of each technique.

Method	Advantages	Disadvantages	Reference
Microemulsion	Simple synthesis	Surfactant and purification required, high polydispersity	Nesamony
Nanomolding	Homogenous and controlled size	Toxic solvents and purification required	Rolland, Garcia
Micro/Nanofluidics	Homogenous and controlled size	Slow particle production and expensive synthesis	Kasianowicz, Hong Zhang
Self-assembly	Simple synthesis No purification	Particle sizes are fixed and unchangeable. Polydispersity usually high	Reddy, Bae, Urakami, Muraoka, Gulseren

It can be seen from this list of methods, that there is still a need for synthesis techniques that can form nanogel particles of different sizes with a low polydispersity using the same starting materials. The described methods suffer from inhomogeneity, difficult synthesis, time consuming purification, and/or inability to adjust particle size. Ideally, it should not be required that a new template or a new polymer be made in order to change the size of the resulting particles. Such constraints slow down synthesis by increasing complexity and raising production costs. Additionally, methods should not necessitate any slow purification steps or expensive materials in order to optimize the process for industrial application of encapsulated biotherapeutics.

Therefore this thesis will outline a new procedure for an optimized nanogel synthesis that meets these requirements. Here we use enzymes to catalyze the crosslinking of biologically derived polymers to form nanogel particles of tunable sizes. Chapter 2 will cover synthesis and analytical techniques used to make and characterize the nanogel particles. Descriptions of instrument basics and data analysis as it pertains to nanogel particles is also outlined. Chapter 3 will relate the results from the synthesis and particle characterization section. Correlations between data and trends observed will be presented in detail. Chapter 4 will discuss the conclusions we drew from the results of our study, the mechanism of nanogel synthesis, and future directions for the study of enzyme catalyzed nanogel particles. Lastly, chapter 5 will summarize the overall ideas presented in this thesis and the broader impact of the findings for drug delivery applications.

CHAPTER 2: SYNTHESIS AND CHARACTERIZATION TECHNIQUES.

2-1) Synthesis of Nanogel Particles.

We hypothesized that nanogel physical gelation could be induced with a synthesis scheme involving the use of 1). A biocompatible polymer that crosslinks in the presence of a specific cation and 2). An enzyme that catalyzes the formation of the specific crosslinking cation. This will allow crosslinking of the nanogels to be controlled by the enzyme's activity as it dictates production of the crosslinker cation.

For the synthesis of nanogel particles, we selected the polymer alginate as our matrix material. Alginate is a biodegradable polymer derived from seaweed that exhibits the ability to ionically crosslink in the presence of certain cations such as calcium and iron (III).[92] These cations have the ability to bind to carboxylate groups and thus create ionic forces between the polymer and ions in a coordinated shape referred to as an "egg box" structure (Figure 2-1).[92]

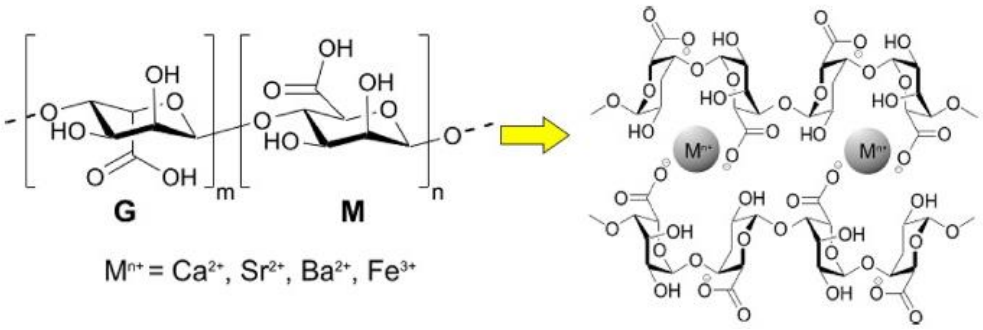

Figure (2-1). Ionically crosslinked "egg box" structure of alginate with specific cations.[92]

The second component used for nanogel synthesis was the laccase enzyme from the fungus *Trametes versicolor.* Laccase was chosen as it has been suggested to have the ability to convert iron (II) cations to iron (III) cations[93,94] which can be used to crosslink the polymer.[92] However, the mechanism of this iron oxidation reaction is not entirely known. Currently, it is not known which forms of iron reactant and product reside in the dissolved solution, iron oxide (Fe_2O_3), iron hydroxide ($FeOH_3$), iron oxide-hydroxide (FeO(OH), or etc. We also hypothesized

in this work that laccase creates the iron III species in a redox reaction. We suggest that it takes an electron from iron (III) and transfers it to oxygen after which the reduced oxygen combines with hydrogen in solution to form water molecules (Figure 2-2). Similarly to other enzyme reactions, the iron conversion reaction in laccase is most likely a multi-step process that generates various intermediate complexes which affect the kinetics of the redox reaction and rate of product formation.[95] Another important quality of laccase is that it creates no deleterious byproducts, only water. This allows for the synthesis of biocompatible nanogels with enzyme catalysis due to the absence of harsh biomolecule degrading components. Furthermore, encapsulation of biological therapeutics will be possible as the synthesis can be conducted in aqueous media, at physiological temperature, and at physiological pH. Since enzyme reactions are easily influenced by parameters such as reactant availability, temperature, and pH, we hypothesize that the use of an enzyme catalyst in nanogel formation will allow us to establish simple control over nanogel crosslinking and thus particle growth kinetics.

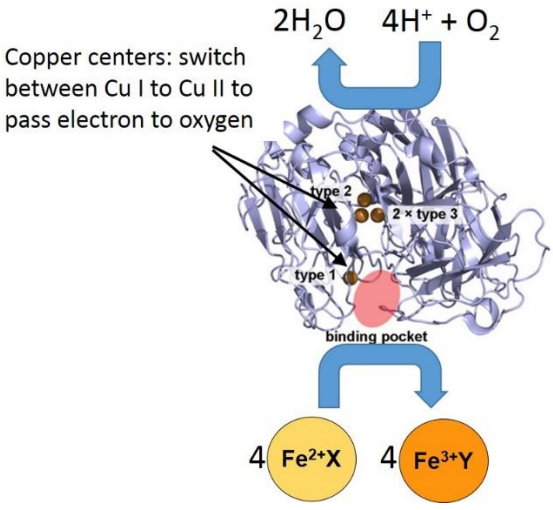

Figure (2-2). Reaction of the laccase enzyme catalyst. Where X and Y are an undetermined anion.

Lastly, we hypothesized that this nanogel synthesis method will allow us to control the size, polydispersity, and density of the particles via simple enzymatic control. All materials and

solvents used for this synthesis are commercially available and biocompatible. It is also easy and quick since it can be conducted in one step. Therefore, we expect that utilizing an enzyme catalyst for the synthesis of nanogels will allow our particles to meet the aforementioned goals of a desirable nanosized drug delivery device.

Chemicals and Reagents. The sodium alginate polymer and laccase from *Trametes versicolor* (E.C. 1.10.3.2) used for nanogel synthesis were purchased from Sigma-Aldrich. Iron (II) sulfate, sodium sulfate, 1,10-phenanthroline, sodium acetate, acetic acid, and phosphate buffer saline (PBS) were purchased from Fisher Scientific. All of the chemicals were used as received and not further purified. All solutions were made with ultrapure water (18.2 MΩ·cm; Barnstead Epure) and experiments performed at ambient temperature, 25°C ± 2 °C. pH of the solutions was measured with an Accumet AB15 Plus pH meter from Fisher Scientific.

Proof of Gelation. To demonstrate gelation and understand the kinetics of bulk gelation, four solutions with different amounts of $FeSO_4$, which was converted by enzymatic activity to iron (III) crosslinker, were monitored. All solutions were made with 0.67 wt% alginate and 0.44 U/ml laccase enzyme in 50 mM sodium sulfate. Additionally, the first solution contained 1.67 mM $FeSO_4$, the second 15 mM $FeSO_4$, and the third 32 mM $FeSO_4$. The fourth sample was a control and contained 0.67 wt% alginate, 0 U/ml laccase enzyme, 15 mM $FeSO_4$, 50 mM sodium sulfate. All solutions but the control exhibited visible gelation at different rates within 24 hours.

Preparation of Films. Enzymatically crosslinked alginate bulk gels were dried to form films. To understand how film properties were affected by iron concentration, samples with varying levels of crosslinker were synthesized. The samples studied contained 0.67 wt% Alginate, 0.44 U/ml laccase, and $FeSO_4$ at concentrations 0 mM, 1.67 mM, and 15 mM. Solutions were allowed to react for 24 hours at room temperature and then dried under vacuum in their reaction containers.

2-2). Characterization with UV-Visible Spectroscopy.

The first technique used to measure the properties of the nanogel particles synthesized in this work was UV-Visible Spectroscopy (UV-Vis). UV-Vis is typically used to determine the concentrations of uv sensitive components in a solution. It accomplishes this by exposing a solution to light and measuring the unabsorbed amount that passes through the solution. The unabsorbed quantity is subtracted from the intensity of the source to yeild the amount of light absorbed by the solution. Frequently, the intensity of absorbance is scanned over different wavelengths to find where peaks occur due to absorbance of certain solution components. Using Beer's law, the concentration of the selected component can be calculated:

$$A = \varepsilon bc \tag{1}$$

where A is absorbance, ε the extinciton coefficient of the absorbing moiety, b the length of solution through which the light passes, and c the concentration of the absorbing component.[96] The extinction coefficient is a value that is usually found in literature, since it can be simply calculated through the use of a concentration calibration curve.

Absorption of light. Absorption occurs in solution when an energy source excites a molecule to a higher energy state (Figure 2-3). In this work, light from a tungsten and deuterium lamp are used in a Thermo Scientific Evolution 600 instrument to excite the sample (Figure 2-4). For the measurements presented in this thesis, two modes of the instrument were used: one where wavelength was held constant over time to measure kinetics, and one where wavelengths are scanned during a fixed amount of time to yeild the absorbtion spectra.

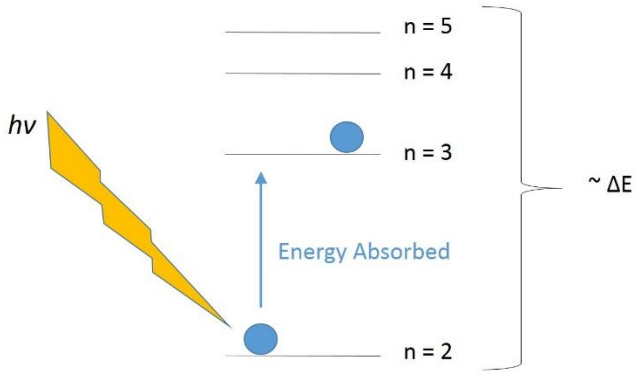

Figure (2-3). Absorption of energy resulting in excitation of a molecule with light.

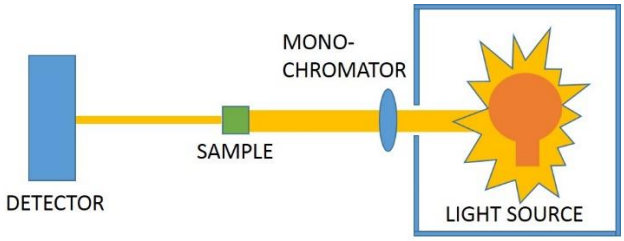

Figure (2-4). Schematic of UV-Vis instrument. A reference may be measured in the sample location and then removed and sample measured. The ratio between the two is analyzed by the software to measure the optical absorption.

2-3). Characterization with Dynamic Light Scattering.

In order to characterize the physically crosslinked nanogels synthesized in this work, one of the techniques used was Dynamic Light Scattering (DLS). DLS is a technique that measures the fluctuations of the refractive index of materials to understand motions in the sample such as the rate of diffusion, conformational flipping, and rotation. By identifying the time scale at which these movements occur, other information about the sample can be determined such as size, shape, density, polydispersity and etc.[97] The nanogel particles synthesized in this study will be examined with DLS to determine their size, shape, and dispersity. DLS works by exposing optically polarizable molecules or particles to a monochromatic light source. The change in their polarizability elicited from their interaction with the wave interferes with the amplitude of the

incident electric field. Due to the direct mathematical relation between electric field and intensity (eq. 6), the intensity measured by the instrument is also altered from the particle wave interaction. So the intensity measured is the light from the source scattered by the interaction with the sample. Another way of understanding scattering is to view the phenomenon as the fluctuation of the local dielectric constant of the medium. Particles are constantly moving in the solution volume which alters the dielectric constant of the illuminated subregion due to the particle's motions.

Scattering data can be used to study translational motion which is measured as particles move in and out of the laser beam path to change its intensity. The scattered light in the experiments used in this thesis was collected at a 90˚ angle with respect to the incident light from a 671 nm solid state laser. It was then collected with a lens and objective and focused into a single mode optical fiber, then split between two avalanche photodiode detectors (Figure 2-5). The use of two detectors allowed the signal to be cross correlated and thus increased the dynamic range and reduced the noise of the instrument.

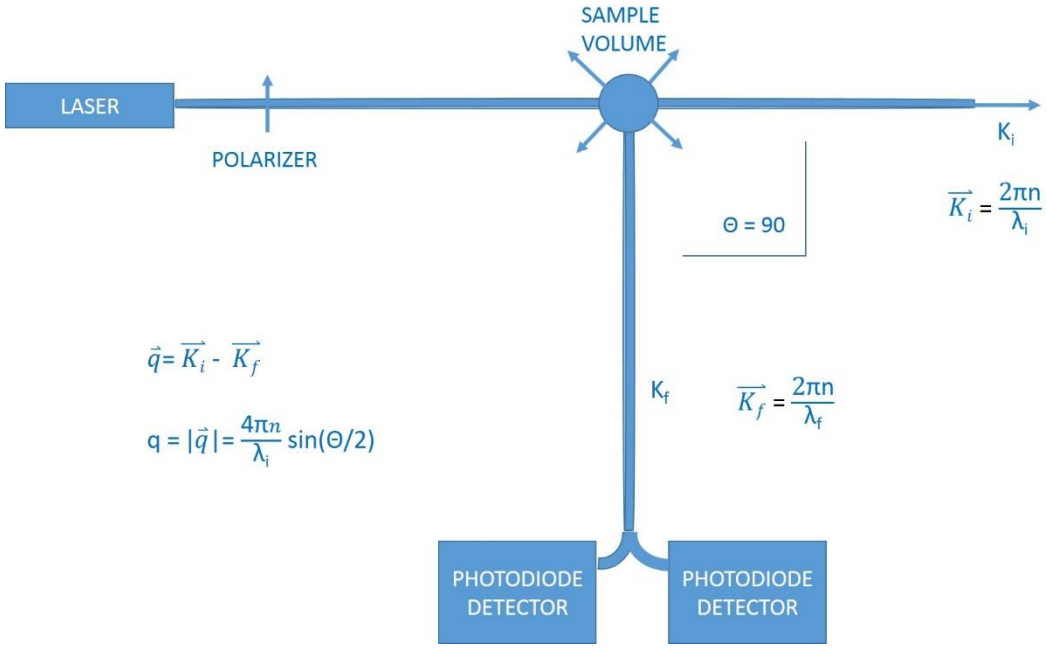

Figure (2-5). Schematic of the DLS set up used. K_f is the wavevector of scattered light, K_i the wavevector of incident light, q the scattering wavevector, n the refractive index of the solution, θ the scattering angle, and λ_i the wavelength of the incident light.

The scattered electric field, E_s, at time t and distance R from the solution can be described using the equation:

$$E(R, t) = ((-k_f{}^2 E_0)/(4\pi R\varepsilon_0))^* \, e^{i(k_f R - \omega_i t)} \delta\varepsilon_{if}(q, t) \quad (2)$$

where E_0 is the field amplitude, ε_0 the average dielectric constant, and ω_i the angular frequency. The last component, $\varepsilon_i(q, t)$, in the equation represents the dielectric constant fluctuation tensor along the initial and final polarization directions.

Analysis of DLS data begins after the detector detects the incoming photons as a pulse. The correlator then calculates the intensity of the scattered light by counting the number of photons as a function of time and performs autocorrelation on the intensity function. Simplified, the autocorrelation function can be understood by the equation:

$$g^2(t) - 1 = \frac{\sum_{t_0=1}^{N-t}(I_{t_0} - \bar{I})(I_{t_0+t} - \bar{I})}{\left(\sum_{t_0=1}^{N}(I_{t_0} - \bar{I})\right)^2} \text{-1} \quad (4)$$

or

$$g^2(t) - 1 = \frac{\langle I(q,t_0) I(q,t_0+t)\rangle}{\langle I(q,t_0)\rangle^2} \text{-1} \quad (5)$$

where q is the scattering wavevector (in this case fixed at 90˚), t_0 is time, t the length of a time segment (lag time),[98] N the number of observations, I the intensity, and $\bar{I}$ the average intensity.[99]

The use of the $g^2(t)$ indicates that the function is second order since intensity is equal to the electric field squared (equation 6) and the lowercase g relates that the function is normalized.[97]

$$I_0 \equiv |E_0|^2 \quad (6)$$

In light scattering, if there is an exact repetition of a sequence of scattering intensity data from particle interference, the autocorrelation value assigned is 1. If there is no repeated pattern in the intensity fluctuations, such as white noise, the value is assigned as 0. These correlation values between 0 and 1 are plotted versus the time length of each repeat sequence (t) called lag time, to form an intensity correlation function (Figure 2-6). The lag time for translational motion can also be understood as the time that it takes for a particle to diffuse through a certain scattering volume. This scattering or illuminated volume occurs at the intersection between the incident and scattered beam.[97]

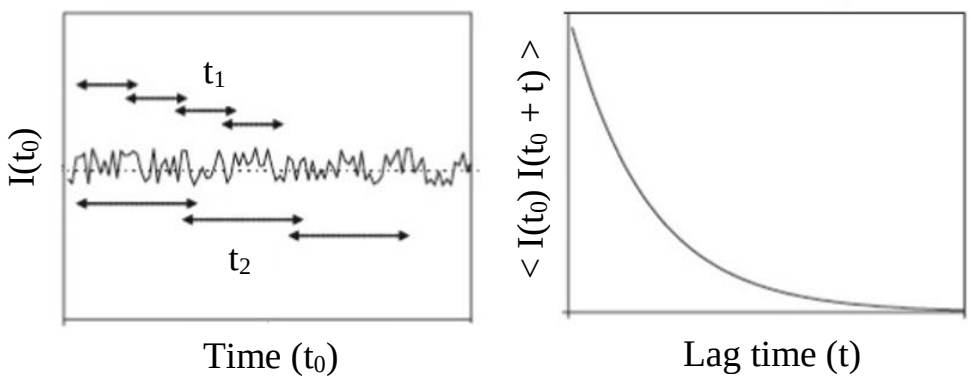

Figure (2-6). Example of how the correlation of intensity data is plotted versus lag time to obtain correlation functions. As the size of t increases, the correlation of the intensity fluctuations decay exponentially.[98]

Measuring Translational Motion with DLS. To measure translational motion, the sample is illuminated with polarized light. When particles begin to move out of the path of the beam, signal correlation intensity drops. This indicates that a specific lag time is related to the diffusion of the particles out of the scattering volume. This specific time length is referred to as the characteristic decay time, or τ_c. This parameter can be determined by fitting the intensity correlation curve with the function determined from taking the Fourier transform of the probability distribution function of finding a particle at a given scattering vector (q) and lag time (t):

$$F_s(q,t) = I(q,t) = e^{\left(-\frac{t}{\tau_c}\right)} \tag{7}$$

Additionally, the decay rate, Γ, for translational diffusion is equivalent to:

$$\Gamma = \frac{1}{\tau_c} = q^2 D_t \tag{8}$$

so that,

$$I(q,t) = e^{\left(-\frac{t}{\tau_c}\right)} = e^{(-tq^2 D_t)} \tag{9}$$

and combining with the Stokes-Einstein equation for translational diffusion,

$$D_t = k_B T / 6\pi\eta R_h \tag{10}$$

can yield the hydrodynamic radius, R_h, of the solvated particle. This parameter may be determined after fitting the intensity data with an exponential decay function like the one shown in equation 9.[97] In the Stokes-Einstein equation, k_B is the Boltzmann constant, T the temperature, and η the viscosity of the solution.

Fitting of Correlation Functions. In this thesis, three types of functions were used to fit the correlated scattering intensity data.

The single exponential decay,

$$g^{(2)}(t) - 1 = \left(A * \exp\left(-\frac{t}{\tau_c}\right)\right)^2 + y_0 \, . \tag{11}$$

The stretched exponential decay,

$$g^{(2)}(t) - 1 = \left(A * \exp\left(-\frac{t}{\tau_c}\right)^{\beta}\right)^2 + y_0 \, , \tag{12}$$

And a function with two decays, the first being a single exponential and the second a stretched exponential.

$$g^{(2)}(t) - 1 = \left(A_1 * \exp\left(-\frac{t}{\tau_c 1}\right) + A_2 * \exp\left(-\frac{t}{\tau_c 2}\right)^{\beta}\right)^2 + y_0. \tag{13}$$

where A is the amplitude of the intensity, t the lag time, τ_c the characteristic decay time, and β the stretching parameter. One reason the β (or stretching) term may be required in the fitting function is that there is a broad distribution of particle sizes in the sample which prevents them from being distinguished. An example of this can be seen in Figure 2-7 where all of the shown decays are components of the normalized stretched decay (pink dashed line). Here, the overall decay curve (pink dashed line) that represents many types of particle sizes is more stretched than its component functions that only represent one particle. Therefore within the one decay curve, there are present a large diversity of correlation times and thus particle sizes which represents polydispersity. The particle polydispersity is represented by the term β in the fitting equation 12 and 13. When β is equal to 1, meaning the function can be fit with a single exponential decay model, then it can be said that all particles are of the same size and monodisperse. This means that all of the particles have the same diffusion coefficient and the same hydrodynamic radius. As β decreases, stretching increases and thus polydispersity of the sample grows. This indicates that the diffusion coefficients and sizes of the particles are varied.[97]

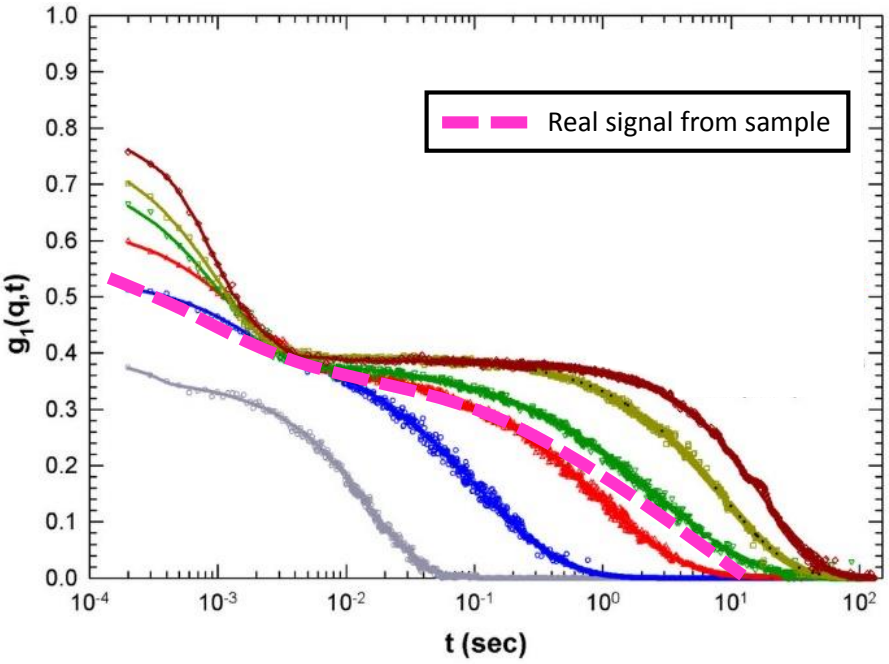

Figure (2-7). Example of how a stretched correlation function is formed. The pink dashed line is an example of the real function that would be seen upon combining all of the other pictured decays. With polydisperse samples the decay function becomes stretched. (Figure modified from Mallamace et al.[100])

2-4). Characterization with Atomic Force Microscopy.

The third technique used to characterize properties of the nanogel particles was Atomic Force Microscopy (AFM). AFM is a technique that is frequently used to complement DLS. It is used to measure the topology of deposited particles and other surfaces. When studying the characteristics of particles it can determine their size, dispersity and height among others. Although the sample size measured by the technique is small, the main advantage of using AFM is that it obtains an image of the sample for visual inspection. Additionally, the image resolution can be on the atomic scale making the technique very accurate.[101]

AFM works by scanning the surface of a sample with a nanosized instrumental tip attached to a flexible cantilever to determine the sample's topography. Attractive and repulsive forces between the tip and sample cause deflection of the tip duing scanning. This deflection is

measured by a laser that is reflected off of the tip onto a detector. Therefore, changes in tip deflection may be detected and interpreted as topography of the sample.[101] In AFM, the type of material and size of the tip used determines the resolution of the image.[102] Here, a silicon tip of <10 nm in diameter was used for imaging.

There are several different modes that can be used to measure a sample with AFM. These are demonstrated in Figure 2-8 and are known as: contact, non-contact, and tapping. Contact mode maps topography by dragging the tip along the sample surface. Forces between the sample and tip measured in this mode are repulsive. The second mode, non-contact, modulates the tip at a resonance frequency and monitors any changes due to attractive force interactions with the sample. As the frequency and amplitude of the tip changes due to force interactions, the computer adjusts the distance between the sample and tip so that the the frequency and amplitude remains constant during scanning. This mode keeps the tip very close to the sample so that the force interactions between them are still measured even though no contact is made.[103] The third mode, Tapping, or intermittent contact mode, is achieved by applying force such that the tip goes in and out of the non-contact and contact mode regions.Therefore in tapping mode both attractive and repulsive force interactions are present between the sample and the tip.

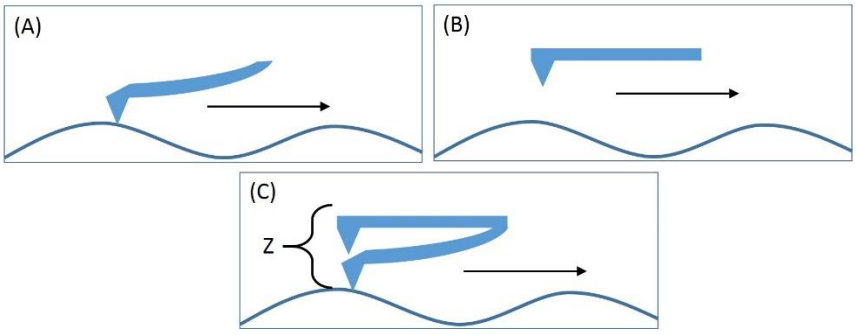

Figure (2-8). Example of the common scanning modes of AFM. (A) Represents contact mode, (B) Non-contact mode, and (C) Tapping mode where the tip oscilates in the Z direction as it scans.

2-5) Characterization with Small Angle Neutron Scattering.

Small Angle Neutron Scattering (SANS) is a technique that works by measuring the scattering signal that originates from interactions between neutron waves and atomic nuclei of sample matter. This causes the resulting scattering intensity to be dependent on the strength of the nucleus-neutron interactions, which is known as the scattering length density (ρ). Due to the relationship between scattering strength and the identity of the atoms that neutrons pass through, SANS can be used to distinguish between isotopes of the same element. Normally hydrogen and deuterium are used for experimental contrast since the scattering length density of hydrogen is much larger than its isotope and the element is plentiful in organic samples. Additionally, hydrogen can be exchanged with deuterium in most samples and the change usually does not significantly affect the system dynamics.[104]

In typical experiments, H_2O and D_2O mixtures are used to view scattering in samples due to their strong differences in neutron-nucleus interactions, identified by the scattering length density (ρ). By changing the percentage of hydrogen and deuterium in a solvent, the experimentalist can effectively tune the scattering length density to be as close to pure H_2O or pure D_2O as desired. This optimizes contrast since it is determined by the difference between the solvent and particle scattering length density:

$$contrast \sim \rho_{particle} - \rho_{solvent} \tag{18}$$

Finding the solvent mixture of H_2O and D_2O that yields the largest difference between $\rho_{particle}$ and $\rho_{solvent}$ is used to maximize the intensity signal scattered from the particles in solution. Furthermore, contrast is very important in SANS because the flux of the neutron source is very low due to the manner in which neutrons are generated for scattering applications. Without proper minimization of background noise, the typically weak signal from the sample may be easily overwhelmed.

One reason why SANS was used in this work is because it allows us to more accurately view our nanogel particles in the semi-dilute regime since it is known that at this concentration they cannot be accurately viewed with DLS. In SANS, the concentration of particles is not problematic because intensity of the scattered signal only depends on the identity of the atomic nucleus (H or D) of the material. Therefore signal from small particles in neutron scattering is

not overwhelmed by signal from large particles so that we can obtain an average size of all of the particles in solution. Another characteristic unique to SANS is that the size range that instruments are able to access typically lies anywhere between 0.5 nm to several hundreds of nanometers, due to the small wavelength of incident neutrons.[105] To see structures of different sizes in this range, the scattering wavevector, q, must be adjusted through manipulation of the scattering angle. The wavevector has an inverse relationship with the probe distance, d, of the sample being examined[106]:

$$q = \frac{2\pi}{d} \tag{19}$$

Therefore, within the q range of the instrument used to study our nanogel particles, 0.00009-0.08 nm^{-1}, the size of objects that can be viewed lies between approximately 0.8-700 nm. Adjusting the wavevector q may be accomplished by changing either the scattering angle θ or the neutron wavelength λ in order to probe different length scales within the sample since:

$$q = \frac{4\pi}{\lambda}\sin(\theta) \tag{20}$$

In figure 2-9, a demonstration of how q is manipulated through variance of sample distance (d_s) from the detector is shown.

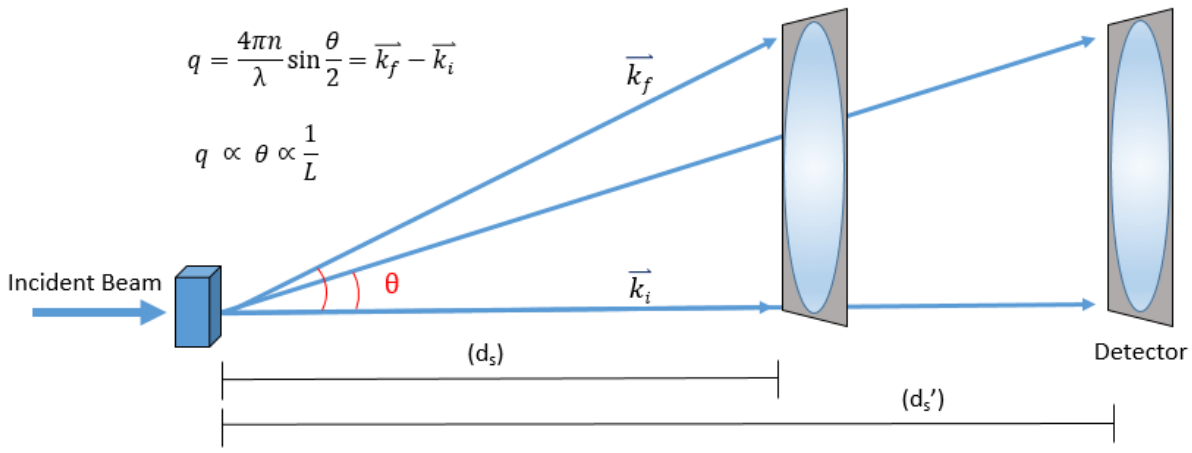

Figure (2-9). A schematic presentation of a typical neutron scattering experiment. As d_s increases, θ decreases, and thus q decreases as well. Here k_f is the scattered wavevector, k_i the incident wavevector.

Analysis. One way to plot neutron scattering data for analysis is to graph the intensity I(q) versus the scattering wavevector q. Since q has an inverse relationship with the probing distance (d), this can give information on the sizes of structures in the solution such as the radius of the particles or the size of the nanogel pores.[107] When q is large, the probing distance is small, therefore the interior structure of the particles (pore size) is being studied. When q is small, the probing distance is large so that the radius of the particles can be viewed.

A change in the slope of the scattering intensity is directly related to the size and shape of the structures in the solution. A change in slope indicates when q has increased enough to switch from probing the whole particle to the interior pore space of the particle. This is due to the relation:

$$I(q) = P(q) * S(q) \tag{21}$$

where P(q) is the form factor and S(q) is the structure factor. The Structure factor S(q) describes the scattering interference between different particles and P(q) the change in scattering from different parts of a single particle. When there is no contribution to interference by interparticle interactions, (i.e. in the dilute regime) S(q) effectively equals 1.[108] Contained within the form factor function is the scattering length density distribution function ρ(r), where r represents position:

$$P(q) \sim \rho(r) \tag{22}$$

The exact relation between P(q) and ρ(r) will be explained later in this section. However, it is important to understand that ρ(r) is dependent on the changes in scattering length density (ρ) that occur as neutrons pass through positions (r) of a sample. The scattering length density is a parameter that represents the inherent scattering strength of a material. So as neutrons scatter from the particles they have a scattering length density of $\rho_{particle}$ and when scattered from the solvent $\rho_{solvent}$. Therefore ρ(r) represents what value ρ becomes when scattering occurs at different positions (r) in the solution:

$$\rho(r) = \rho_i \delta(r - r_i) \tag{23}$$

where $\rho(r)$ represents the scattering length density distribution function, ρ_i the scattering length of the relevant material, and r position.[108] In Figure 2-10, the change that occurs in scattering

length throughout a sample is demonstrated. Furthermore, it represents an example of how contrast tuning with H_2O and D_2O is utilized to enhance ρ from selected components (solute or solvent) in solution. In (A) the scattering length of the solvent is set to be low and in (B) the scattering length of the solute is said to low. This change in p(r) directly alters the form factor P(q) which in turn changes the intensity I(q) of scattering from either the solute or solvent. This allows the experimentalist to maximize signal from either the particles (solute) or pores (solvent) through contrast adjustment while using the same analysis method to analyze the results.[104]

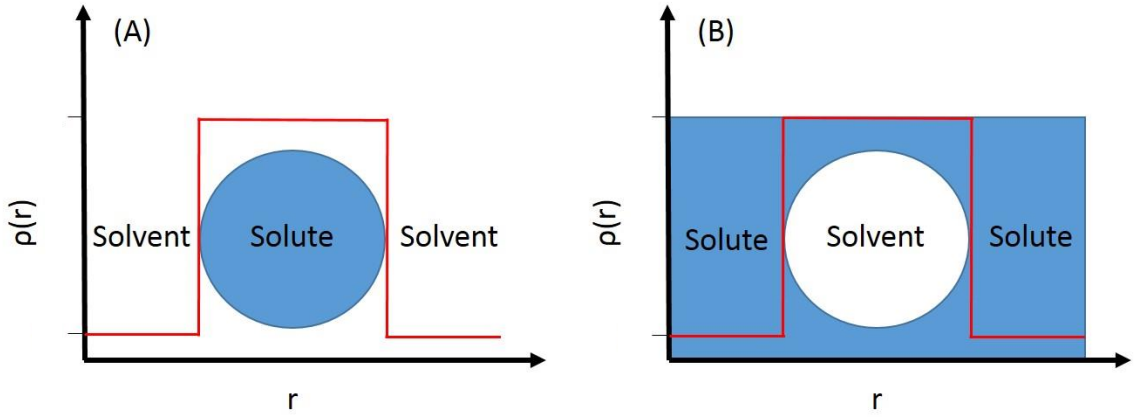

Figure (2-10). How scattering length fluctuates as neutrons interact with different parts of the solution. Scenario (A) is when the particles are being analyzed at low q and (B) when pores are being analyzed at high q. The scattering length density of either solute or solvent may be set to the lower value using contrast adjustment with H_2O and D_2O.

Low q Analysis. To find the radius of the nanogel particles, q must be sufficiently small. This area, called the Guinier region, occurs when:

$$q \ll \frac{1}{R_g} \tag{24}$$

By plotting ln (I(q)) vs q^2, the slope of the data in the Guinier region can be used to determine the radius of gyration without knowing the shape of the structures using the equation[108]:

$$ln\big(I(q)\big) = ln\big(I_{bkg}\big) - \frac{q^2 R_g^2}{3} \tag{25}$$

where I_{bkg} is the initial intensity from the background. An example of the Guinier region and how it can be used to find particle size is shown in Figure 2-11.

High q Analysis. To determine the structure of the gel pores, analysis was performed in the high q or Porod regime which is defined to occur when:

$$q \gg \frac{1}{R_g} \tag{26}$$

In this regime, unlike in the Guiner regime, the form factor P(q) is dependent on shape and internal stucture of the particles. Therefore an equation that relates the scattering intensity per unit volume, I(q), to the volume fraction, , φ, and the form factor P(q) is used:

$$I(q) = \varphi P(q) + I_{bkg} \tag{27}$$

where I_{bkg} represents the incoherent scattered background. To determine information about the particles in this size scale, the shape and therefore the density distribution function, of the structure must be known.[104] Shown in Figure 2-11 is an example of the Porod region from neutron scattering data and how it depends on shape and internal structure. However, for our particles, the density distribution function was not known, so a different fitting approach had to be utilized. To describe the hierarchy that exists in polymer gels, a generalized Porod's law was used to relate structural information.[110]

$$P(q) = \left(\frac{\left[erf\left(\frac{qR_g}{\sqrt{6}}\right)\right]^3}{q}\right)^P \tag{28}$$

where *erf* is the error function, *q* the scattering wavevector, *Rg* the radius of gyration, and P the Porod exponent. This approach applies a generalized scattering function to the data to limit the parameters used in fitting so that it may relate structural information over a wide range of q

values. Other more specific models were attempted to fit the data, but the parameters obtained from the fits were not physically relevant or did not contribute meaningful information to the analysis without further experimentation.

Instrument Configuration. Small Angle Neutron Scattering was carried out at the CG-3 Bio-SANS instrument located in the High Flux Isotope Reactor (HFIR) at the Oak Ridge National Laboratory (ORNL) with a Q range of 0.00009-0.08 nm^{-1}.[105] Two instrument configurations were used to cover a wide range of scattering vectors, $0.0003 < q < 0.04$ nm^{-1}, i.e., sample-to-detector distances of 2.529 m and 15.329 m with a fixed λ of 0.6 nm. The instrument resolution was defined by the placement of circular apertures (diameters), 40 mm as source and 14 mm as sample, at a separation distance of 17.430 m. The area detector, 1 m x 1 m GE-Reuter Stokes Tube detector used for collecting scattering and transmission data, was offset by 400 mm from the beam center for the experiment. Data reduction and analysis were performed using the IgorPro software package.[105,112] Raw 2D images were processed by normalizing to incident beam monitor counts and correcting for detector dark current, pixel sensitivity and subtracting cell background scattering.

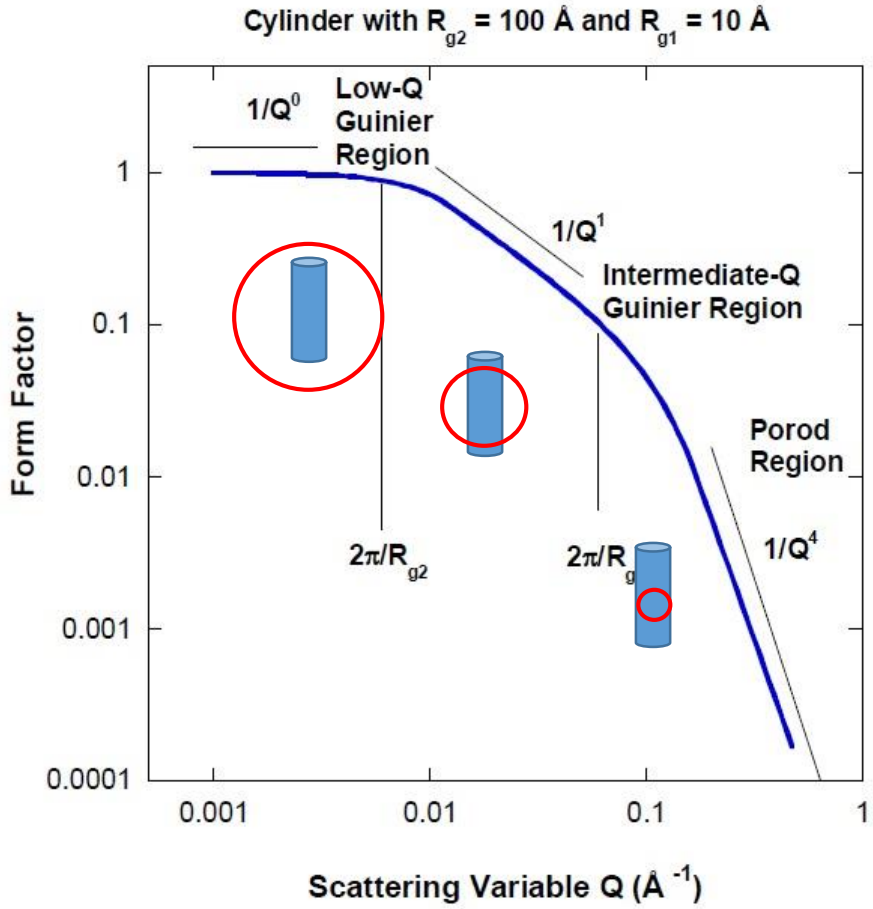

Figure (2-11). An example of how the form factor P(q) changes with q for cylindrical particles. The red circle represents how the probed distance (d) changes with q variation.[107]

2-6). Characterization with Viscometry and Rheology.

To find the viscosity of the solution studied in DLS, mixtures containing different concentrations of alginate were studied with viscometry and rheology. This provides a good estimate of overall solution viscosity because alginate is by far the most viscous component of the nanogel synthesis reactants, with the others contributing negligibly. Due to differences in fluidity of dilute and concentrated alginate solutions, two techniques were used to determine their viscosity: Ubbelohde Viscometry and Rheology.

Ubbelohde Viscometry. Viscometers measure solution viscosity by measuring the amount of time it takes for a solution to travel between two calibrated distances.[113] Our dilute alginate solutions were studied with this technique. Using the Hagen-Poiseuille Law, the volumetric flow rate can be related to viscosity, η:

$$\frac{V}{t} = \frac{\pi R^4 \Delta P}{8L\eta} \tag{30}$$

where V is volume, t is time, R the radius of the tube and L the length of the tube. The pressure change, ΔP, is equivalent to the product of the density of the solution (ρ), gravitational acceleration (g), and the height of the mean hydrostatic pressure (h_m):

$$\Delta P = \rho g h_m \tag{31}$$

Here we assumed that ρ for the solution was the same as water since the percent of polymer we chose to study remained below the dilute limit. During experiments, volume was held constant so that the only unknowns to be determined were viscosity, η, and time, t. Therefore, the viscosity of the solution can be found by taking the ratio of time (t_0) to viscosity (η_0) of the solution and comparing it to that of water (t_w and η_w):

$$\frac{\eta_0}{t_0} = \frac{\eta_w}{t_w} \tag{32}$$

Rheology. Rheology is the second technique we used to measure solution viscosity. It calculates viscosity through measurement of the strain and stress of a material.[114] Due to the high viscosity and thus low flow rate of concentrated (above the dilute limit) alginate, measurements

of 1 wt% polymer were determined with a rheometer instead of Viscometry. Rheometers measure viscosity by applying stress (creep test) or strain (startup shear) forces to a sample wedged between two mechanical plates in a chamber at a controlled temperature. The first quantity measured by the instrument, shear rate ($\dot{\gamma}$ or strain rate), is defined by:

$$\dot{\gamma} = U/h \tag{33}$$

where *U* is the velocity of the top plate in the x direction and *h* the height difference between the plates. The second quantity, shear stress (τ or stress), is defined by:

$$\tau = F/A \tag{34}$$

where F is the shear force on the top plate, and A the area of the sample in contact with the plate. Taking the ratio of these two yields the viscosity of a solution[115]:

$$\eta = \tau/\dot{\gamma} \tag{35}$$

The way viscosity is measured for polymers is through the zero shear viscosity value ($\boldsymbol{\eta_0}$) determined via a rheological creep measurement (Figure 2-12). Creep experiments apply a fixed stress to the material and measure the resulting strain over time. When the strain rate reaches equilibrium, the zero shear viscosity can be found using[116]:

$$\eta_0 = \tau_0/\dot{\gamma}_0 \tag{36}$$

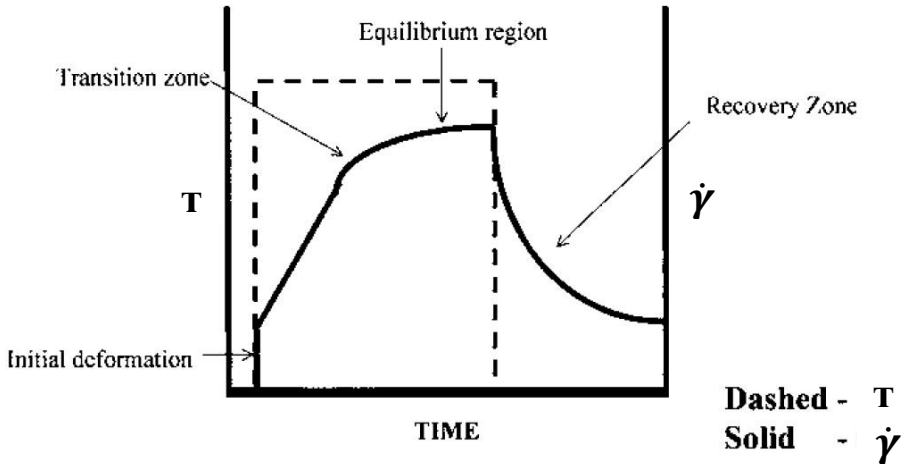

Figure (2-12). Example of a creep experiment. Where the dashed line represents the applied stress (τ) and the black line the resulting strain rate ($\dot{\gamma}$) of the material. When the curve reaches equilibrium at the top, the zero shear viscosity can be determined.[117]

Combining the viscosity values found from both viscometry and rheology, a curve of viscosity versus concentration can be plotted. When concentration of a polymer solution is extrapolated to zero from this calibration curve, intrinsic viscosity [η], can be found. This value is useful because it allows for the calculation of the polymer mass using the Mark-Houwink equation for an aqueous alginate solution[118]:

$$[\eta] = 0.035M^{0.66} \tag{37}$$

where the value 0.66 in this equation is specific to the polymer-solvent pair and temperature. The radius of gyration, R_g, for our alginate polymer was found using the Fox Flory equation[113]:

$$R_g = \sqrt[3]{[\eta] * \frac{M_w}{\phi}} \tag{38}$$

where$[\eta]$ is the intrinsic viscosity, ϕ the Fox Flory constant, and M_w the polymer molecular weight.

Viscometry and Rheology Experimentals. The viscosity of several alginate solutions with different weight percentages were determined. Viscometry was used to measure the dilute solutions, and rheology was used to measure the concentrated 1 wt% solution. For the dilute

solutions, a Cannon-Ubbelohde Dilution Viscometer, model B941, was used at 18˚C for characterization. To calculate viscosity of the alginate solutions, the flow time of the alginate solution was compared to that of pure water. Creep shear measurements were performed on an AR2000ex rheometer for the concentrated 1 wt% alginate solution under the stress of 10 Pa at 18˚C. To ensure accuracy of the measurements, a cone plate with a diameter of 60 mm, cone angle of 2˚, and truncation length of 49 μm were selected for use.

CHAPTER 3: RESULTS

3-1). Enzymatic Induced Gelation.

3-1-1). Enzyme Kinetics

Iron (III) Formation in Buffer. The kinetics of iron (II) oxidation in buffered solutions was studied using UV-Vis. The absorbance of enzyme containing soultions was monitored at 400 nm for 20 min. The samples consisted of 50 mM sodium acetate buffer, 0.72 mM iron (II) sulfate, and different concentrations of laccase (0, 0.1, 0.5, and 1 U/ml). The iron (II) sulfate was added to the solution just before measurements of the iron (III) acetate complex began. A pH of 6 was mantained throughout the experiment in order to optimize enzyme activity and prevent iron precipitation. Afterwards, an identical experiment was run except that all solutions were made in D_2O so that the kinetics could be compared to the samples in H_2O to complement the analysis of later collected neutron scattering data.

Results. In buffered acetate solution made with water, our results show a plateau in iron conversion rates after 10 minutes with a solution of 1 U/ml laccase, after 20 minutes with 0.5 U/ml laccase, and no plateau with 0.1 U/ml laccase within the 20 minute window. Such variances demonstrate that the speed of the reaction depends on the amount of laccase at the represented concentrations (Figure 3-1).

The results from an identical experiment performed in D_2O are also shown in Figure 3-1. It can be seen that enzyme activity in D_2O is reduced, however, overall the system produces more iron (III) acetate. This means that the enzymatic reaction in D_2O takes longer to saturate so that it reaches a much greater absorption maximum. It was also observed that oxidation of iron by ambient oxygen in solution (black lines Figure (3-1)) was reduced in the D_2O environment. These results were used to help elucidate data collected later by neutron scattering experiments.

Iron (II) Dissapearance. To further confirm iron conversion, a second experiment was run where the consumption of iron (II) instead of production of iron (III) was measured. 1,10-

phenanthroline is known to bind to iron (II) to form a complex that absorbs at 508 nm. A stock solution consisting of 50 mM acetate buffer, 0.72 mM iron (II)sulfate, and 0.5 U/ml laccase was assembled. Approximately every 2 minutes a 100 µl aliquot of solution was drawn and mixed 100 µl of (0.167 mM) 1,10-phenanthroline in 1.8 ml of water. A second sample with no laccase was run parallel to the first as a control. Resulting iron (II) concetrations were calculated using the Beer-Lambert law and the molar extinction coefficient of $\varepsilon_{512} = 11.1\ mM^{-1}\ cm^{-1}$.[119]

Results. It was found that disappearance of iron (II) during a reaction with 0.5 U/ml laccase was significant in comparison to the control sample, (Figure 3-2 (A)) confirming enzymatic conversion. Therefore we can firmly claim that laccase catalyzes the conversion of iron (II) to iron (III) based on our UV-Vis studies.

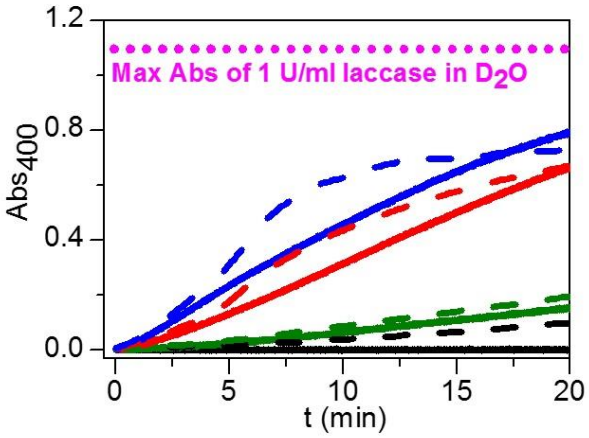

Figure (3-1) Absorbance of iron (III) acetate complex at 400 nm, pH 6.0. Solid lines represent samples in D_2O and dashed lines in H_2O. Samples additionally contain laccase concentrations of 0 U/ml (black), 0.1 U/ml (green), 0.5 U/ml (red), and 1 U/ml (blue). The pink dotted line represents the max absorbance of 1 U/ml laccase in D_2O at its plateau (occurs at a time not featured).

Oxygen Limitation. To observe the effect that oxygen (an enzyme reactant) has on the kinetics of the reaction, a similar experiment was run under argon (Figure 3-2 (B)). Two separate solutions containing 50 mM acetate buffer and 0.5 U/ml laccase and 0.72 mM iron in water were bubbled with argon gas for 20 minutes before combining and measuring kinetics. Midway during the reaction, the sample was mixed throughly to reincorporate oxygen into the solution and observe the change in kinetics.

Results. It was found that argon saturation significantly slowed enzyme activity and that it could be recovered with re-oxygenation. This assay shows that the enzyme reaction can be easily controlled by substrate (oxygen) availability. Furthermore, it means that the production of iron (III) crosslinker in solution can be easily tuned via the enzyme reaction and thus affect the kinetics of nanogel particle growth.

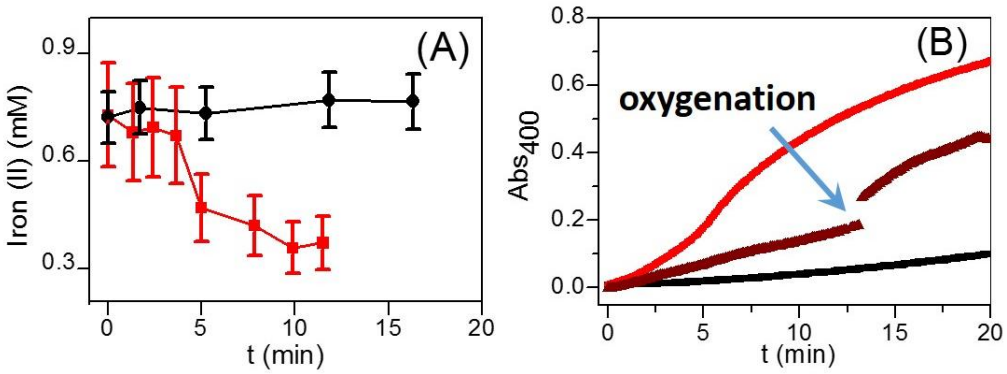

Figure (3-2). Graph (A) shows the concentration of iron (II) calculated from the absorbance of the iron (II) 1-10 phenanthroline complex at 508 nm. The black line is a control with 0.72 mM iron (II) sulfate in 50 mM acetate buffer and the red line sample additionally 0.5 U/ml laccase. Graph (B) shows a sample containing 0.72 mM iron sulfate and 0.5 U/ml laccase in 50 mM acetate buffer, pH 6 under argon (dark red line) and ambient atmosphere (red line). The arrow indicates the point at which the mixture was stirred to oxygenate the solution. The black line is a control with the same components, but no laccase.

3-1-2). Polymer Molecular Weight

Another property of the solutions studied was viscosity. The viscosity of several alginate solutions, 0.02 wt%, 0.035 wt%, 0.05 wt%, 0.07 wt% and 1 wt% were determined. Measurements were repeated five times each to reduce error. Molecular weight of the polymer was calculated from the viscosity measurements of the alginate solutions (Figure 3-3). The intrinsic viscosity [η], was found to be 1340 ml/g and the maximum polymer molecular weight 333 ± 23 kg/mol from the Mark-Houwink equation for alginate solutions (eq. 37). The maximal radius of gyration for alginate in solution was found to be 32 nm using the Fox-Flory equation (eq. 38). However this number will vary from the radius of gyration determined from SANS measurements as it measures the average value instead. Due to the large polydispersity of the alginate polymer, the maximal and average radius of gyration should be different.

3-1-3). Gelation.

Gelation of the bulk material was also explored. Since gelation/crosslinking can not occur without iron (III) present, the speed of the gel formation can be attributed to the speed of iron (II) oxidation with or without the laccase catalyst. Here we investigated gelation due to iron conversion in an aqueous solution under an air atmosphere. It was found that gelation rate of a solution could be slowed with decreasing amounts of iron crosslinker. It was found that when combined with 0.67 wt% alginate and 0.03 mg/ml (0.44 U/ml) laccase, a sample with 32 mM iron showed bulk gelation after 6 hours, 15 mM after 18 hours, and 1.67 mM no gelation within 24 hours. A control sample without laccase only exhibited signs of gelation after 3 weeks in solution indicating laccase accelerated the oxidation rate of iron (II) greatly.

These samples were then dried under vacuum at room temperature until the water was completely removed and films were formed. A slight yellow tint colored the films due to iron (III) content. Additionally, the clarity of the films varied based on the amount of iron in the solution (Figure 3-5). As the iron content increased, the more transparent the films became. We speculate that this change in transparency is due to the amount of water in the dried films. Free iron (III) is known to be hydrophobic in solution. Therefore, as iron (III) content increased in solution, more water may have been driven out of the film.

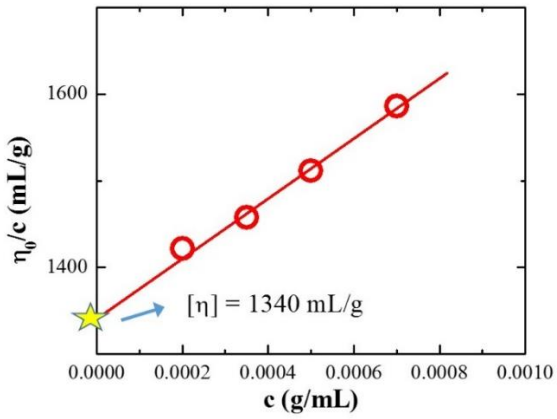

Figure (3-3). Viscosity data plotted versus concentration, c, to estimate the intrinsic viscosity [η].

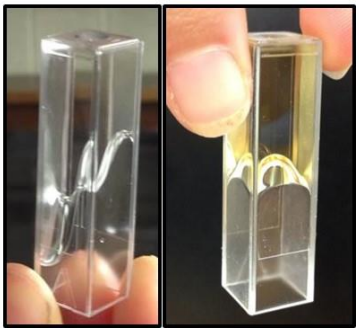

Figure (3-4). Demonstration of bulk gelation. Alginate and iron in the absence (A) and presence (B) of laccase enzyme.

Figure (3-5). Films synthesized with 0.67 wt% alginate, 0.03 mg/ml (0.44 U/ml) enzyme and iron (II). The films are overlaid on top of the words in the bottom right corner. Iron concentrations are 0, 1.67, and 15 mM which correspond to samples labeled: 0, 100 µl and 900 µl.

3-2). Enzymatic Production of Nanogel Particles.

3-2-1). Dynamic Light Scattering.

Experimentals. DLS was used to study the dynamics of the particle's growth in solution. It allowed for the calculation of particles sizes, particle polydispersities, and particle growth rates. The solution studied with DLS was within the dilute limit for polymers, meaning that the polymer coils were well separated in solution and not entangled. Below the dilute limit it is known that the formation of nanoparticles is favored in solutions.[120] The limit at which solution viscosity may no longer be considered dilute was calculated using[121]:

$$\rho^* = \frac{R_g M 3}{N_A 4\pi} \quad (14)$$

where ρ* is the viscosity at which polymers become entangled, R_g the radius of gyration, M the molceular weight of the polymer, and N_A Avogadro's number. The amount of polymer used for these experiments was below ρ* indicating that measurements were performed on a dilute solution.

To examine if particle growth kinetics could be controlled, two concentrations of crosslinker precursor (iron II) were studied in solutions. To synthesize nanogel particles, a solution was prepared of the following components: 0.07 wt% sodium alginate, 0.187 U/ml laccase enzyme, and 0.0714 M Na_2SO_4. These were run through 0.22 μm polyethersulfone filters 2-3 times until the dust particles and large aggregates were removed from the solutions. A stock solution of $FeSO_4$ was filtered separately and added to the sample for final concentrations of 0.36 mM and 3.6 mM. Scattering measurements were initiated at the time of iron sulfate addition. Intensity data was collected in one minute increments by the instrument and the intensity correlation function was calculated with an ALV-7004/USBFAST digital correlator. Functions were fit with equations 11-13 and hydrodynamic radius calculated using equations 9 and 10. The viscosity of water (1.33 cp) was used in the Stokes equation to calculate particle hydrodynamic radius.

Results. It was found that solutions containing 0.014 mg/ml (0.187 U/ml) laccase enzyme, 0.07 wt% alginate, and 0.36 and 3.6 mM iron exhibited changes in nanogel particle size

and polydispersity during the growth cycle. The correlation functions of the particles in solution over time can be viewed in Figure 3-6 (A and B). Throughout the growth process, three distinct regions were observed and were fitted with 3 different correlation functions (Figure 3-7). The first function was a stretched exponential decay and is shown in equation 11. The second function was a single exponential decay and is demonstrated in equation 12. The last function consisted of two exponentials, a stretched decay and a single decay and is shown in equation 13. Using the characteristic decay time found from the fittings, the diffusion coefficients of the particles in solution were calculated (eq. 9). Using the Stoke-Einstein equation (eq. 10), the hydrodynamic radius of the particles was calculated from the diffusion coefficients.

When the hydrodynamic radius of the particles was plotted versus time, three distinct regions of growth appeared during nanogel formation (Figure 3-8). Region I is an area where slow or no growth occurred. Region II is an area where a fast increase in particle size manifests. Lastly, in Region III, particle growth tapers off and in the case of the 3.6 mM iron sample, also splits into two separate processes.

Additionally, the polydispersity of the particles was measured via the beta exponent, or stretching parameter of the correlation functions. The stretching of a function indicates the presence of multiple sizes of particles. It is also plotted in Figure 3-8 to show how stretching/polydispersty changes depending on the growth region. Both samples were found to have a low beta, or high polydispersity, in region I. However, after region I, growth begins in earnest and beta quickly jumps up near 1 indicating the formation of nearly monodisperse populations of particles toward the end of region II. Region III exhibits a high beta, or low polydispersity. However, in the 3.6 mM iron sample, a second process (shown in red in Figure 3-8) was formed that was very polydisperse in nature. In the case of the 0.36 mM sample, the second highly polydisperse process never develops so that beta remains high and polydispersity of particle sizes low.

It is also interesting to note that as the iron concentration increased, the time in which it took the particles to reach a monodisperse size was reduced. By increasing the availability of iron (II) cations by ten times, the speed of the growth process increased by ten times. For the 0.36 mM sample, region III was reached at 1600 minutes whereas for 3.6 mM it occurred at ~300 minutes, demonstrating a dependence of the speed of particle growth on the availability of iron crosslinker. Overall, nearly monodisperse populations of alginate nanogel particles were

formed from samples with two different concentrations of iron. For 0.36 mM iron, particle polydispersity remained very low between 34 and 44 nm and in the case of 3.6 mM iron between 47 and 100 nm.

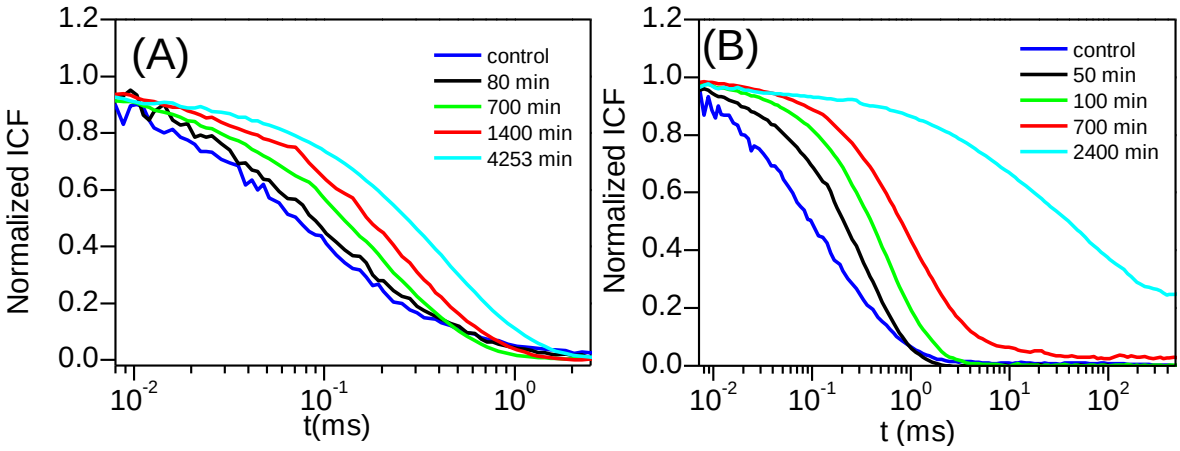

Figure (3-6). Change in the normalized intensity correlation functions of (A) 0.36 mM iron and (B) 3.6 mM iron over time.

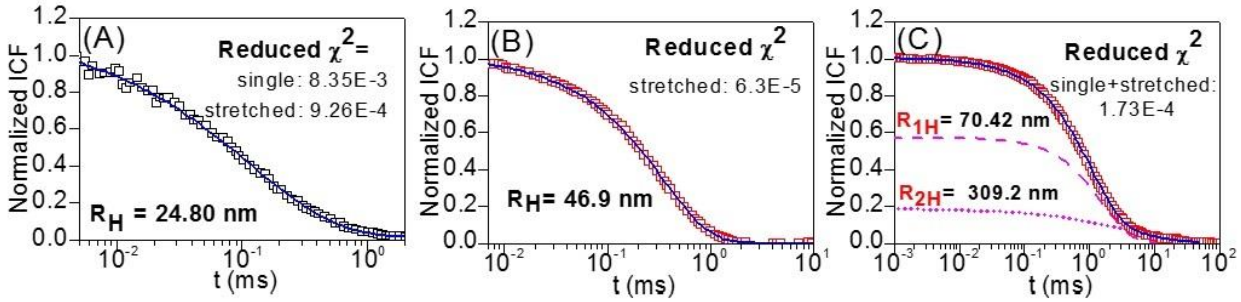

Figure (3-7). The three types of correlation functions observed throughout nanogel growth. These were fit with equations 11-13 (stretched exponential, single exponential, and single exponential + stretched exponential) and the hydrodynamic radius (R_H) was calculated with the Stokes-Einstein relation (eq. 9). The reduced χ^2 value represents the quality of the fit when used with the specified equation.

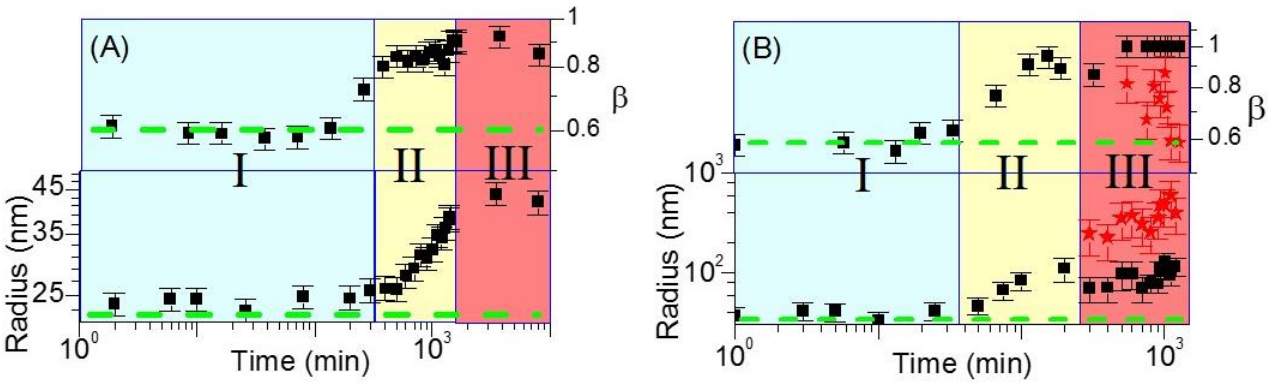

Figure (3-8). (A) Change in the hydrodynamic radius and stretching parameter, β, (polydispersity) of the particles over time when synthesized with (A) 0.36 mM iron and (B) with 3.6 mM iron. The three regions are marked as I, II, and III. The red points in (B) represent a second process that develops only in region III of the 3.6 mM iron sample. The dotted green line is a base line representing the size of particles present in a control sample with no iron.

3-2-2). Atomic Force Microscopy.

Experimentals. Samples for AFM analysis were synthesized by combining 0.07 wt% alginate, 0.262 U laccase, and 0.36 and 3.6 mM Fe_2SO_4 in 0.0714 M $NaSO_4$ solution. Stock solutions were left to react and aliquots withdrawn at different time intervals to image the growth process as it occurred. Samples were deposited and dried on a silica substrate for AFM analysis. AFM of nanogel particles was performed in tapping mode of the commercial instrument, Asylum Cypher. Collected images were analyzed with the WSxM image analysis program. Using cross-section analysis, the width and height of the particles were determined.

In AFM, two artifacts from the instrument usually appear during scanning: broadening of the particle size due to the tip shape and height lowering of particle size due to elastic deformation. Profile broadening of particle radius occurs because the tip has finite width and thus the reported size of the particles from the instrument is composed of the real width of the particle convoluted with the width of the tip (Figure 3-9). Therefore the radius of the particle must be deconvoluted from radius of the tip using the equation:

$$r_c = 2\sqrt{R * r} \tag{16}$$

where r_c represents the distance between the center of the tip and center of the particle, R the radius of the tip, and r the radius of the particle.[122] We assumed that height of the particles was negligibly affected by deformation since the measurements were taken in tapping and not contact mode. It was assumed that deposition caused surface confinement of the hydrophilic particles and forced them to form spherical cap shapes.[123] Therefore, the volume of the non-deposited particles was calculated using the assumption that the volume of the spherical cap was equal to the volume of a sphere:

$$V_{sphere} = \frac{4}{3}\pi r^3 = \frac{1}{3}\pi h^2(3r - h) = V_{cap} \tag{17}$$

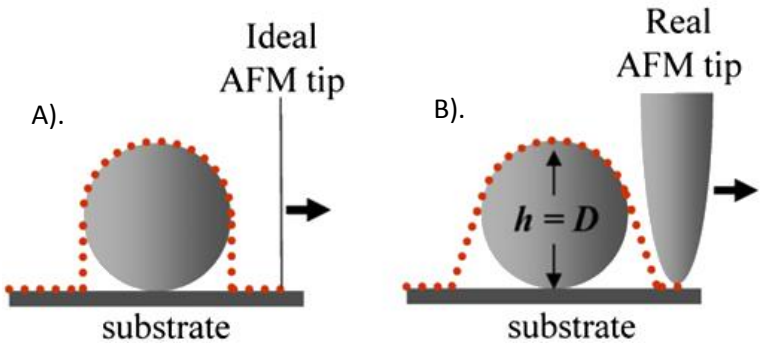

Figure (3-9). Tip broadening due to A). a tip with no width (ideal = no tip broadening), and B). a tip with width (real).[124]

Results. Using AFM, the nanogel growth process was captured in two different regions, II for 0.36 mM iron and III for 3.6 mM iron. The size distributions in Figure 3-10 (C) and (D) correlate with the DLS results in Figure 3-8 (A and B). From the image of the 3.6 mM iron particles (Figure 3-10 (B)), it can be seen that when imaged in region III, aggregation was indeed the reason why a second process in DLS appeared.

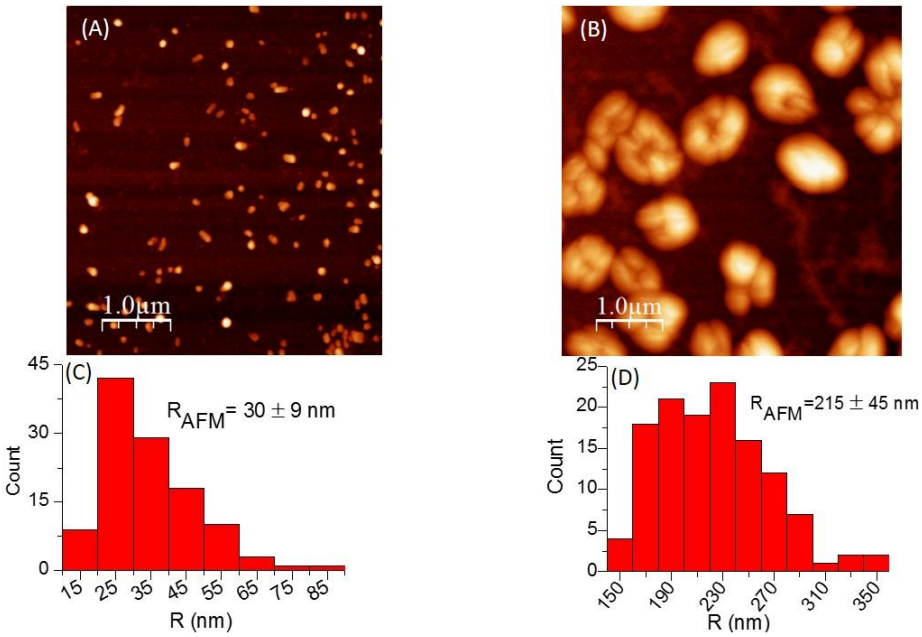

Figure (3-10). AFM images and size distributions of nanogel particles diluted 50 times from their original solutions. The growth process of the 0.36 mM sample was imaged in regime II (A) and the 3.6 mM sample in regime III (B). The size distributions are shown in (C) and (D) for their respective images.

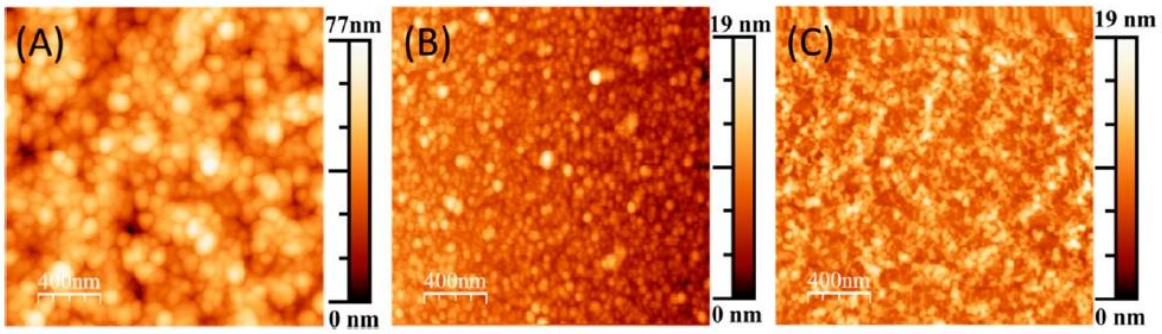

Figure (3-11). (A) shows the nanogel particles after 60 min of reaction with 3.6 mM iron. B) is a control with only laccase (0.187 U/ml), and C) a control containing laccase (0.187 U/ml) and alginate (0.07 wt%) but no iron.

Additional confirmation of the association of the second process with aggregation was obtained through independent estimates of the average distance between nanogel particle centers in solution. Calculation of the average distance between particle centers was conducted under the assumption that each enzyme seeds the growth of an individual particle. So that enzyme concentration is the reagent that limits the number of particles seeded in the solution. The total solution volume was 1.4 ml and the enzyme concentration 0.187 U/ml (equal to 3×10^{-10} mol based on molecular weight of ca. 66 kDa for fungal laccases[125] or N = 1.8×10^{13} particles in this volume). The conversion from milligrams to units of enzymes was done based on a conversion factor of 13.1 U/mg supplied from the manufacturer. To find the approximate maximum radius that particles can grow to without touching each other, referred to as the distance between particle centers $\langle d \rangle$, the following equations were used:

$$\langle d \rangle = 2R \tag{39}$$

where R is the particle radius and

$$V = \frac{4\pi}{3} R^3 * N \tag{40}$$

where N represents number of particles (found by assuming each enzyme seeds one particle) and V the solution volume. This estimates the maximum radius before the particles come into contact to be ~123 nm. Interestingly, this number is in good agreement with the radius obtained from our experimental data (Figure 3-8 (B)) as the size at onset of aggregation lies around 100 nm. These findings indicate that the nature of the second process found in DLS is likely an aggregation of particles due to crowding.

3-2-3). Small Angle Neutron Scattering.

Experimentals. Samples were soaked in either 100% D_2O or 100% H_2O solvents and then filled into quartz banjo cells (Hellma) with path lengths of 2 mm and 1 mm, respectively. Concentrations of components in samples were: 0.22 U/ml laccase, 0.22 wt% alginate, and 1.5,

15, and 45 mM $FeSO_4$. Once mixed, the particles were allowed to grow undisturbed for 24 hours before measurement with SANS.

Small Angle Neutron Scattering was performed on the system in the semi-dilute regime to see if enzymes could still form nanoparticles at higher alginate concentrations. Small angle neutron scattering profiles of the alginate gels show measureable structural differences as a function of Fe^{2+} ion concentration, from 1.5 to 15 to 45 mM (see Figure 3-12). Alginate gel samples were prepared and studied in two solvents, 100% H_2O and 100% D_2O. A subset of alginate gel samples formed with 1.5 and 15 mM of Fe^{2+} ions were studied in both solvents because the use of 100% D_2O solvent alleviates two important drawbacks: (1) low scattering signal of the sample; and (2) high incoherent backgrounds from hydrogen atoms. The approach to alleviate the first drawback relies on increasing scattering contrast between the sample and solvent and the latter by replacing solvent hydrogen atoms with deuterium atoms. On the other hand, the use of 100% D_2O potentially introduces detrimental artifacts such as a higher propensity for aggregation due to the enhanced activity of the enzyme in this solvent (shown in the UV-Vis results, Figure 3-1). Therefore, it is imperative to study representative samples in both 100% H_2O and 100% D_2O solvents to understand the function of solvent identity in particle growth.

To determine the overall particle size and pore size of the nanogels, a graph of I(q) versus q was produced by azimuthally averaging the 2d images about the beam center position. The resulting curve was fit with the Single level Unified model[111] in the IRENA package[126] as it was the best approach to extract reliable information from the system[110]:

$$I(q) = \left[G * exp\left(-\frac{q^2 R_{g\,part}^2}{3} \right) + B * \left(\frac{\left[\mathrm{erf}\left(\frac{q R_{g\,pore}}{\sqrt{6}} \right) \right]^3}{q} \right)^P \right] + I_{bkg} \qquad (29)$$

where G is the scalar for the exponential component, $R_{g\,part}$ is the radius of gyration of the nanogel particle, $R_{g\,pore}$ is the radius of gyration of the nanogel pore, B is the scalar for the power-law scattering component, P the Porod exponent, and I_{bkg} is the background intensity with incoherent scattering as its predominant component. This model was selected because it fitted the intensity profile found for the nanogel particles and produced the most applicable interpretation of fitting parameters. It consists of a unified Guinier and Porod model which contains an

exponential form at lower q, representative of a particle size followed by a power-law profile with the Porod exponent reflecting the particle's bulk properties such as polymer particle architecture, conformation, density, shape, and pore size. The results of the fit for all the samples are summarized in Table 3-1.

Results: Guinier/Low q Regime. The Guinier component of the Unified model primarily fits the experimental data in the low-q regime to provide the radius of gyration of the structures. In this region, only the samples in 100% H_2O could be fit with the model to find a particle size as no exponential component was observed in the 100% D_2O samples within the studied q range. This trend indicates that larger particles are formed in the 100% D_2O solvent than in the 100% H_2O solvent. In the H_2O based samples, particle size, R_g, was found to increase with increasing Fe^{2+} ion concentration. A 3-fold increase in Fe^{2+} ion concentration (15 to 45 mM) resulted in the particle size doubling, R_g increased from ~20 to 40 nm, or an 8-fold increase in particle volume if we assume a spherical shape. The smallest measureable average particle size, R_g ~ 20.8 nm, is much larger than the average size of the protein (2.5 nm)[127]. This implies that free enzyme is not present in the solution and is most likely entangled within the nanogel polymer matrix after the growth of the particles is complete.

Results: Porod/High q Regime. The power law profile in the high-q regime provides the Porod exponent which gives information on the interior structure of the nanogel particles. It is used to characterize the fractal structure of a gel.[109] Shown in Table 3-1, nanogels of all iron concentrations exhibited branched structures since their power law exponents fell between 2 and 3. Porod exponents for other structures such as swollen coils (P = 5/3) and collapsed spheres (P = 3) were not observed.[107] This branching indicates that the nanogel structure is a porous material that is more dense than swollen polymer coils but less dense than hard polymer spheres. The variation in Porod exponents demonstrates that the nanogel material has the potential for tunable porosity in addition to tunable particle size.

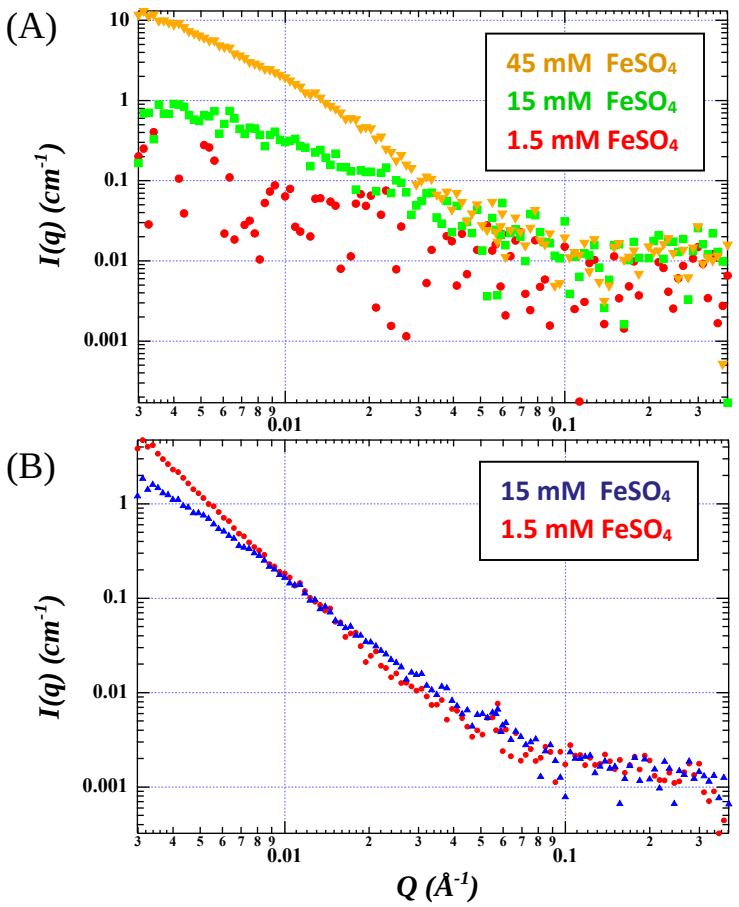

Figure (3-12). SANS spectra of alginate gel in solvents: (a) H_2O and (b) D_2O as a function of Fe^{2+} ion concentration ranging from 1.5 to 45 mM.

Table (3-1). Fit parameter values of the single level unified model.

Buffer	Concentration (mM)	G (cm^{-1})	R_g (Å)	B ($1.0E^{-5}$ cm^{-1})	P
H_2O	45	19.01	397.2	2.31	2.480
	15	0.8746	207.7	2.31	2.173
D_2O	15	–	–	0.55	2.234
	1.5	–	–	0.04	2.808

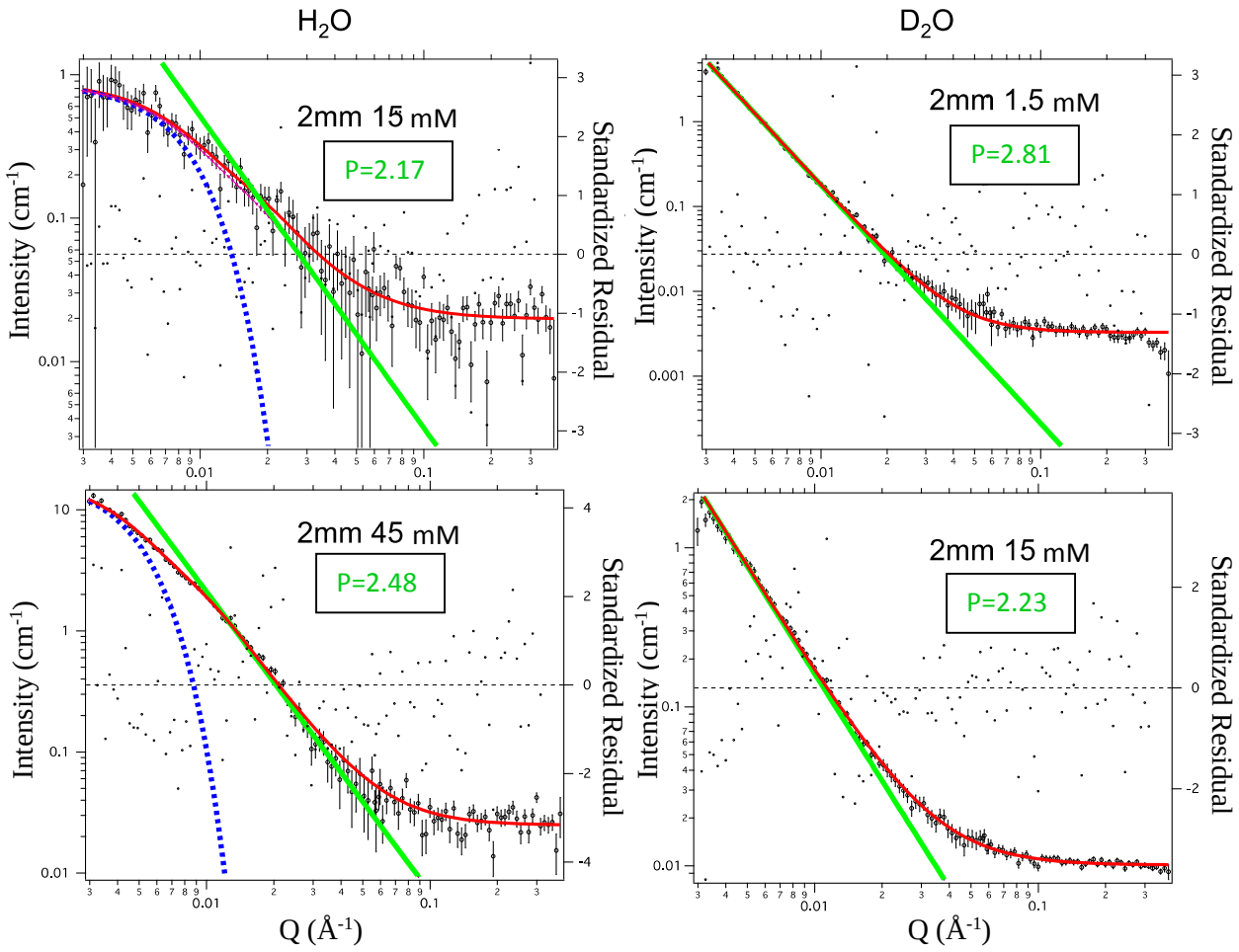

Figure (3-13). Unified model fitting. Blue lines represent the Guinier fit and green the Porod law. In the D_2O samples, no Guinier fit could be placed as there was no exponential behavior of the samples at low q.

CHAPTER 4: DISSCUSION

4-1). Mechanism of Nanogel Growth.

In this thesis, it was hypothesized and proven that nanogels could be synthesized utilizing enzyme catalysis to control crosslinking of polymers through ionic charge condensation interactions. In our synthesis method we chose to use the enzyme laccase and the polymer alginate crosslinked with iron. We showed that the synthesis method is reliant on laccase presence as no gelation in solution occurred without it. The growth of the nanogel particles was clearly witnessed in the DLS results in Figure 3-8 to give proof that our goal was achieved. The kinetics of our nanogel's growth demonstrate that the enzyme is a key component in the synthesis mechanism and that three distinct regions of growth exist in particle formation. To the best of our knowledge, the kinetics of nanogel synthesis with an enzyme catalyst has not previously been investigated in literature. Understanding the mechanism of nanogel development is a key component to establishing control over the particle growth process. This will allow the size of nanogel delivery carriers to be tuned appropriately for use in medical applications.

Laccase Catalyzes Particle Growth. It is evident in this synthesis method of alginate nanogel particles that the enzyme in the solution serves as a catalyst for particle formation and growth. Without the enzyme in the solution, iron oxidation occurs slowly and gelation is only witnessed after several weeks of incubation. In solutions with laccase enzyme, gelation was shown to occur within several hours given the proper reactant concentrations indicating that a catalyst is present to drive the gelation process forward.

Growth Region I. Due to the use of an enzyme catalyst, the growth kinetics of our nanogel particles are quite unique. Based on the DLS results in Figure 3-8, it can be seen that there are three distinct regions of particle growth. In the first area, Region I, little to no growth of the particles is evidenced. One explanation for this occurrence is that intermolecular crosslinking between polymer chains has not yet occurred. This may happen because the iron (III) being produced by the enzyme is being sequestered through intramolecular crosslinking within individual polymer chains. Furthermore, it has been shown from our UV-Vis results that laccase

does produce significant amounts of iron (III) early in the growth process. Therefore, the reason why no growth is occurring should not be related to the enzyme's production of iron, but to the mechanism of iron crosslinking in solution. Instead we suggest that in region I: all of the produced iron is being solely used for intramolecular crosslinking within polymers so that no growth of the particles is observed during this time. Another possible explanation for the lack of growth in region I may be that the growing particles remain too small to be seen during this region as their scattering signal is masked by larger polymer coils in solution.

Growth Region II. In this region fast particle growth was observed. We hypothesized that the increase in particle size is due to intermolecular crosslinking between polymer chains. Here, as particles grow via assumed attachment/crosslinking of free polymers, the polydispersity of the particles rapidly decreases. One reason why the particle size increases may be that the amount of iron needed to complete intramolecular crosslinking has been used up and that the excess iron (III) produced by the enzyme can now be used to intermolecularly bond polymer chains. Furthermore, in region II, polydispersity decreases which presumably indicates that the free/unbound alginate polymers (with smaller diameters than the particles) are being taken up by the growing particles to create a more homogenous overall particle size distribution in solution.

It is also assumed that in this step, that enzymes become trapped within the nanogel particles as more polymers are added to them. The addition of polymers to the particle should hinder enzyme diffusion through the particle matrix. Furthermore, laccase enzymes have been shown to exhibit an affinity for iron substrates[128] and may very well associate with iron (III) crosslinker in the nanogel particles.

Region III. In region III of the growth cycle, there appears a first process in both the 0.36 mM and 3.6 mM iron samples where growth of the particles levels off and polydispersity remains constant. This may be considered the maximum monodisperse particle size that can be attained with the given amount of reactants in solution. However, in the 3.6 mM sample, there appears a second process in region III. The second process seen is hypothesized to result from aggregation of the growing particles. This was confirmed with AFM as images revealed several nanogel particles stuck together as the dominant state in this phase. Other clues that support this thought are our critical threshold calculations from the results section that calculate similar

critical sizes ~123 nm and the suddenness of the onset of the second process which is typical of aggregation behavior.[129]

Overall Growth Kinetics. Putting all of these ideas together offers us a picture of what the growth mechanism of our nanogel particles may look like (Figure 4-1). During region I, the alginate chains are using iron (III) produced by the enzyme to undergo intramolecular crosslinking within themselves. Once all of the intramolecular sites are filled, iron begins intermolecularly crosslink with freely diffusing alginate polymers. This signals the beginning of region II of the growth process where an increase in particle size and subsequent decrease in polydispersity occurs. Polydispersity is seen to decrease because all of the free alginate polymer coils are being used up so that less coils are present to broaden the size distribution of the solution since they are smaller than the particles. In region III, the growth of the particles levels off as all of the iron in the solution is consumed. However, in the case of the sample that contained 3.6 mM iron (II), the crosslinker was not used up once the maximum particle size was reached. This caused the crowded particles to continue their growth via aggregation. Thus a sharp increase in polydispersity arises as particles quickly aggregate due to continued iron crosslinker production and crowding.

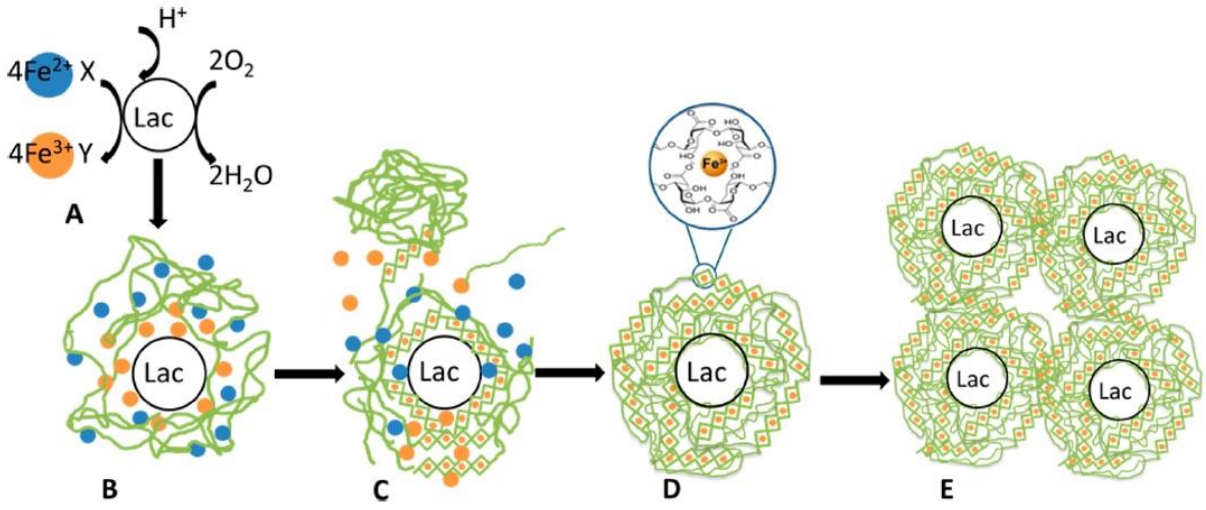

Figure (4-1). Proposed mechanism of nanogel particle growth. Shown in (A) is the general enzyme catalysis reaction. (B) is a representation of region I and demonstrates intramolecular

crosslinking (C) is a representation of region II and shows intermolecular crosslinking between several alginate polymers resulting in increasing particle size. (D) represents the particle after crosslinking has completed (region III) and before aggregation begins. (E) represents the second process in region III, where aggregation of the fully grown nanogel particles occurs.

4-2). Tuning Nanogel Particles.

In this work, it was also hypothesized that the nanogel particle kinetics could be easily tuned with simple parameters such as environmental conditions and reactant concentrations. We effectively showed that size, polydispersity, density, and growth speed of the particles could be controlled in this manner. The two environmental parameters we used to alter enzyme activity included: oxygen absence and incorporation of deuterated water as a solvent. The synthesis components whose concentration was changed to study their effects on nanoparticle growth include: alginate, iron, and laccase enzyme.

Oxygen Availability. Oxygen availability was shown to have a significant effect on the rate of oxidation of iron (II). Here we demonstrate that laccase activity is diminished when there is less oxygen present during synthesis (Figure 3-2). For the enzymatic oxidation of iron (II), oxygen gas is a reactant that is believed to receive the electron removed from iron (II) ions. This is important because it demonstrates that this parameter may be used to alter the kinetics of nanogel growth. In the future, it would be beneficial to know if other environmental conditions that affect enzyme activity, such as temperature and pH, may be used to control nanogel particle kinetics. This may offer an easy way to terminate nanogel growth in order to dictate the resulting size of the grown particles.

Deuterated water. We found that deuterated water also affects particle kinetics by slowing iron conversion and increasing resulting particle size. The deceleration of iron (II) conversion to iron (III) is shown in the UV-Vis results and the increase in particle size in the SANS results. The difference in sizes of particles synthesized in D_2O versus H_2O most likely stems from the higher level of iron (III) produced in deuterated water (Figure 3-1). With more

iron present, the attachment of free polymers to the growing particles can be extended. This demonstrates the concept that higher concentrations of crosslinker can create larger particles if excess polymer is present. Currently, we have no explanation regarding why D_2O affects the enzyme reaction so drastically. However, we speculate that there are certain enzymatic intermediates that may inhibit iron conversion less in heavy water than in normal water.

Alginate Concentration. Controlling the concentration of alginate polymer allowed us to create nanogels instead of bulk hydrogels. This can occur because as long as plentiful alginate and crosslinker are present, the polymer in solution will continue to crosslink until particle crosslinking reaches a scale large enough to be considered bulk gelation. Using ~10 times less alginate (0.07 wt% instead of 0.67 wt%) in solution allowed the formation of nanogel particles as opposed to bulk hydrogels. It is well known that formation of nanoparticles is favored in dilute solutions.[130] Interestingly, our particles still formed while in the semi-dilute regime in the SANS experiments. This is most likely due to the enzymatic nature of our synthesis scheme. Even in bulk gels, it is known that enzyme catalyzed gel formation creates certain local areas of more densely crosslinked polymers.[131] One reason this may happen is because enzymes can create uneven distributions of crosslinker in solution. This results from the restriction of their movement due to entrapment in the growing polymer matrix during the growth process. When the enzymes are confined within crosslinking polymers, the iron concentration near that area naturally increases as the enzyme continues to produce crosslinker. This may be a factor that drives nanogel formation even in a semi-dilute polymer solution.

Iron Concentration. The amount of iron in the solution was shown to affect nanogel speed of growth, size, density, and aggregation. The first outcome of increased iron concentration was an increase in the speed of nanoparticle formation. We believe that the speed of the reaction increases with higher iron concentrations because there is more iron (III) present in solution. The speed of the laccase enzyme reaction does not limit the oxidation of iron. Otherwise, increasing the iron (II) concentration would have no effect on the resulting iron (III) presence. This would cause amounts of iron (III) to remain the same no matter how much iron (II) is added to the solution. However, it seems that in our system, diffusion to the enzyme active site is what limits the amount of iron (III) produced as amounts can be increased upon iron (II)

addition. This is evidenced in Figure 3-8 when the 0.36 mM iron (II) sample reaches it maximum particle size at ~3000 minutes, and the 3.6 mM iron (II) reaches its peak size at ~300 minutes.

Secondly, size of the nanogels can be controlled with iron concentration. Polymers attach to the nanoparticle via crosslinking, so if the amount of crosslinker is increased, then attachment is increased, and the particle size is increased (seen in the DLS results). However, growth of particle size due to iron concentration can only occur when excess polymer is present. Without extra polymer, the particles will only aggregate when extra iron is introduced as there is nothing more left to crosslink in the solution besides the particles themselves.

Thirdly, the density of the interior structure of the nanogels was controlled by iron concentration. This can be seen in the SANS results where the Porod exponent fluctuates with iron variation. Currently, we have no explanation or suppositions regarding this density change. However it is significant and should be noted that this parameter can be controlled through iron concentration.

Lastly, iron concentration controls the onset of aggregation in nanogel particle growth. This is seen in the DLS results when the sample with 0.36 mM iron shows no aggregation, but the 3.6 mM does. Aggregation may occur for two reasons. 1). because the particles become too crowded in the solution to continue growing and begin to link with one another and 2). because the free polymer has been used up so that iron crosslinker begins to bind particles together instead. In the first scenario, particles may form aggregates because the solution reaches a critical threshold where there is no more room for growth and thus the particles must bind to one another to continue the growth process with iron crosslinker. In the second scenario, aggregation occurs because the polymer concentration is limited so that excess iron crosslinker begins to bind particles together instead of free polymer. Understanding where this critical aggregation threshold lies will be important to the creation of precise sizes of nanogel particles with this synthesis method in the future.

Enzyme Concentration. We found that laccase concentration affects the speed of iron conversion from the UV-Vis results and likely the size of the nanogel particles in solution. Although we did not collect data to see if a relationship between increasing enzyme concentration and particle size exists, literature supports this hypothesis. In a recent paper by Silva et al., the authors synthesized bulk hydrogels crosslinked by enzyme catalysis and studied

them with SANS. They showed that their gel was inhomogenous due to enzyme presence and exhibited clusters of densely crosslinked regions that were attributed to enzyme activity. Furthermore, they showed that as the amount of enzyme increased in a sample, the size of these dense clusters correspondingly increased.[131] Therefore, we assume that our particles will act in a similar manner where increasing enzyme concentration leads to larger particle sizes.

Summary. Overall it can be seen from the results presented in this work that altering concentrations of synthesis components can have a drastic effect on nanogel formation kinetics. The enzymatic nature of our synthesis scheme allows the size, polydispersity, density, and speed of nanogel particle formation to be easily regulated. A summary of how specific synthesis components change the growth kinetics of nanogel particles is listed in Table 4-1. Furthermore, additional control over the reaction can be exerted using environmental parameters, such as oxygen availability and solvent type, making this method finely tunable to the needs of specific medical applications.

Table (4-1). Effects of component concentrations on the growth of nanogel particles when they are limiting (+) and in excess (-) based on their discussion in chapter 4.

Component	Limiting Reagent	Limiting Reagent	Limiting Reagent
Laccase	+	-	-
Alginate	-	+	-
Iron	-	-	+
Controlled Properties	1). Size of particles	1). Dictates whether gel or nanoparticles 2). Size of particles	1). Speed of particle growth 2). Propensity for aggregation. 3). Density of gel particle matrix 4). When < aggregation size, controls particle size

4-3) Assessment of Drug Delivery Capability.

The experiments and results demonstrated here show how the nanogel growth reaction can be controlled with synthesis conditions and components to create monodisperse drug delivery particles for future biomedical applications. The nanogels synthesized in this thesis are good delivery systems for biotherapeutics because they can be grown to sizes below 100 nm, allow for simple size tunability, and have a low size distribution. Furthermore, they meet other requirements for successful drug delivery devices such as: utilization of biodegradable/biocompatible materials, lack of toxic synthesis components, simple synthesis, and inexpensive materials.

From the dynamic light scattering results, we demonstrate that particles can be grown to 45 nm within 3000 minutes and 100 nm within 300 minutes using two different concentrations of iron sulfate. Additionally, the polydispersity of sizes can be forced to remain low by limiting iron (II) availability in solution. We also showed that oxygen presence (another enzyme reactant) influences enzyme activity which leads us to believe that nanogel sizes may be affected by this parameter and others that adjust enzyme reaction speed, such as temperature and pH. Another important finding from our experiments was that the limit at which aggregation occurred (for solutions containing 0.187 U/ml enzyme and 0.07 wt% polymer) lies somewhere between concentrations of 0.36 and 3.6 mM iron.

In the future, finding at what concentration the aggregation limit occurs will enable the accurate synthesis of particles with low polydispersity for increased drug delivery efficiency. Also, another factor that should be explored in future studies is how to improve the mechanical strength of these nanogels. Typically, charge condensated materials rapidly dissolve in aqueous environments. This causes them to release encapsulated drugs quickly. For extended drug release and targeting applications, these particles might be modified with protective coatings for future biomedical applications.

CHAPTER 5: CONCLUSIONS

Here we demonstrate the synthesis and characterization of enzyme catalyzed nanogel particle formation. Using laccase enzymes, alginate polymers, and iron (II) sulfate purchased commercially, the synthesis can be carried out in one pot, one step, and completed in a single day. In this thesis, the focus of our experimentation was to see how concentrations of synthesis components and environmental conditions can be altered to tune the size and polydispersity of nanogel particles.

One of the components that was used to control nanogel size and polydispersity was the concentration of iron (II) in solution. Nanogels made with different iron concentrations were characterized extensively with several techniques. Dynamic light scattering was used to capture the growth kinetics of the particles in real time. It was found that their size and polydispersity varied depending on the stage of growth in which the particles existed. Furthermore, once the particles grew to their maximum size, their polydispersity remained low when aggregation was not present. Atomic Force Microscopy was used to image the particles during the growth cycle to verify the DLS results. They revealed corresponding particle sizes and aggregates as confirmation. Small Angle Neutron Scattering was used to determine how size and density/porosity of the particles changes with iron concentration in the semi-dilute region. It was found that the size of the particles in water was similar to DLS, but not in D_2O as the particles were significantly larger. Density of the internal particle structure was also shown to change with iron concentration and solvent type. Lastly, UV-Visible spectroscopy revealed that the laccase enzyme is the catalyst that drives nanogel formation. The appearance of iron (III) and disappearance of iron (II) were significantly enhanced due to enzyme activity and were found to be affected by oxygen and D_2O presence.

Our results show that this method of enzyme catalyzed nanogel synthesis offers considerable control over nanogel particle growth kinetics. By changing conditions such as iron (II) concentration, oxygen concentration, and D_2O presence, the size, growth speed, density, and polydispersity of the particles may be regulated. This supplies the experimentalist with many tools that are easy to use in order to control the size of these nanogel particles.

In summary, this thesis has divulged a method with which to grow nanogel particles with tunable sizes below 100 nm using enzymatic catalysis. To the best of our knowledge, this

investigation documents the first account by which nanogel particles cross-linked via enzyme activity have been achieved without previous polymer modification.[132] These particles are good candidates for drug delivery carriers as they have low polydispersity, sizes below 100 nm, and are synthesized with a simple one-step method. Furthermore, application of these materials to the biomedical profession is facilitated by the use of biocompatible and inexpensive materials, solvents, and reactants.

REFERENCES

(1) X. M. Lam, E. T. Duenas, A. L. Daugherty, N. Levin, J. L. Cleland. Sustained Release of Recombinant Human Insulin-like Growth Factor-I for Treatment of Diabetes. *Journal of Controlled Release*, **2000**, 67, 281–292.
(2) R. M. Williams, J. Shah, Brandon D. Ng, Denise R. Minton, Lorraine J. Gudas, Christopher Y. Park, and Daniel A. Heller. Mesoscale Nanoparticles Selectively Target the Renal Proximal Tubule Epithelium. *Nano Lett.* **2015**, 15, 2358−2364.
(3) D. Shenoy, S. Little, R. Langer, M. Amiji. Poly(ethylene oxide)-Modified Poly(β-amino ester) Nanoparticles as a pH-Sensitive System for Tumor-Targeted Delivery of Hydrophobic Drugs. 1. In Vitro Evaluations. *Mol. Pharm.* **2005**, 2(5), 357–366.
(4) V. P. Torchilin, A. N. Lukyanov, Z. Gao, and B. Papahadjopoulos-Sternberg. Immunomicelles: Targeted pharmaceutical carriers for poorly soluble drugs. *PNAS*, **2003**, 100(10), 6039-44.
(5) M. Longmire, P. L. Choyke, H. Kobayashi. Clearance Properties of Nano-sized Particles and Molecules as Imaging Agents: Considerations and Caveats. *Nanomedicine (Lond)*. **2008**, 3(5), 703–717.
(6) S. V. Vinogradov, T. K. Bronich, A. V. Kabanov. Nanosized cationic hydrogels for drug delivery: preparation, properties and interactions with cells. *Advanced Drug Delivery Reviews*, **2002**, 54, 135–147.
(7) S. A. Kulkarni, S. Feng. Effects of Particle Size and Surface Modification on Cellular Uptake and Biodistribution of Polymeric Nanoparticles for Drug Delivery. *Pharm Res.* **2013**, 30, 2512–2522.
(8) W. H. De Jong, W. I. Hagens, P. Krystek, M. C. Burger, A. J. Sips, R. E. Geertsma. Particle size-dependent organ distribution of gold nanoparticles after intravenous administration. *Biomaterials*. **2008**, 29(12), 1912-9.
(9) G. Zhang, Z. Yang, W. Lu, R. Zhang, Q. Huang, M. Tian, L. Li, D. Liang, C. Li. Influence of anchoring ligands and particle size on the colloidal stability and in vivo biodistribution of polyethylene glycol-coated gold nanoparticles in tumor-xenografted mice. *Biomaterials*, **2009**, 30(10), 1928-36.
(10) A. Elbakry, E. C. Wurster, A. Zaky, R. Liebl, E. Schindler, P. Bauer-Kreisel, T. Blunk, R. Rachel, A. Goepferich, M. Breunig. Layer-by-Layer Coated Gold Nanoparticles: Size-Dependent Delivery of DNA into Mammalian Cells. *Small.* **2012,** 8(24), 3847–3856.
(11) B. Alberts, A. Johnson, J. Lewis, M. Raff, K. Roberts, P. Walter. *Molecular Biology of the Cell.* 4th ed.; Garland Science: New York, 2002.
(12) H. Y. Nam, S. M. Kwon, H. Chung, S. Y. Lee, S. H. Kwon, H. Jeon, Y. Kim, J. H. Park, J. Kim, S. Her, Y. K. Oh, I. C. Kwon, K. Kim, S.Y. Jeong. Cellular uptake mechanism and intracellular fate of hydrophobically modified glycol chitosan nanoparticles. *Journal of Controlled Release.* 135(3), **2009**, 259–267.
(13) M. L. Tsai, Shi Wei Bai, Rong Huei Chen. Cavitation effects versus stretch effects resulted in different size and polydispersity of ionotropic gelation chitosan–sodium tripolyphosphate nanoparticle. *Carbohydrate Polymers*. 71(3), **2008**, 448–457.
(14) M. G. Weimuller, M. Zeisberger, K. M. Krishnan. Size-dependant heating rates of iron oxide nanoparticles for magnetic fluid hyperthermia. *Journal of Magnetism and Magnetic Materials*. **2009**, 321(13), 1947–1950.

(15) S. F. Sweeney, Gerd H. Woehrle, and James E. Hutchison. Rapid Purification and Size Separation of Gold Nanoparticles via Diafiltration. *J. Am. Chem. Soc.*, **2006**, 128 (10), 3190–3197.
(16) C. Sanson, C. Schatz, J. F. Le Meins, A. Brûlet, A. Soum, S. Lecommandoux. Biocompatible and Biodegradable Poly(trimethylene carbonate)-b-Poly (L-glutamic acid) Polymersomes: Size Control and Stability. *Langmuir*. **2010**, 26(4), 2751–2760.
(17) L. Tang, J. Azzi, M. Kwon, M. Mounayar, R. Tong, Q. Yin, R. Moore, N. Skartsis, T. M. Fan, R. Abdi, J. Cheng. Immunosuppressive Activity of Size-Controlled PEG-PLGA Nanoparticles Containing Encapsulated Cyclosporine A. *Journal of Transplantation.* **2012**, 2012.
(18) K. Jabłczyńska, M. Janczewska, A. Kulikowska, T. R. Sosnowski. Preparation and Characterization of Biocompatible Polymer Particles as Potential Nanocarriers for Inhalation Therapy. *International Journal of Polymer Science*. **2015**, 2015.
(19) N. S. Berchane, K. H. Carson, A. C. Ficht, M. J. Andrews. Effect of mean diameter and polydispersity of PLG microspheres on drug release: experiment and theory. *Int J Pharm*. **2007** 337(1-2), 118-26.
(20) A. Budhian, S. J. Siegel, K. I. Winey. Controlling the *in vitro* release profiles for a system of haloperidol-loaded PLGA nanoparticles. *International Journal of Pharmaceutics*. **2008**, 346(1-2), 151–159.
(21) A. Seelig, R. Gottschlich, R. M. Devant. A Method to Determine the Ability of Drugs to Diffuse Through the Blood-brain Barrier. *Proc. Natl. Acad. Sci. USA.* **1994**,91, 68-72.
(22) J. Seidler, S. L. McGovern, T. N. Doman, B. K. Shoichet. Identification and Prediction of Promiscuous Aggregating Inhibitors among Known Drugs. *J. Med. Chem.* **2003**, *46*, 4477-4486.
(23) C. Hansch, J. P. Björkroth, A. Leo. Hydrophobicity and central nervous system agents: On the principle of minimal hydrophobicity in drug design. *Journal of Pharmaceutical Sciences*. **1987**, 76 (9), 663–687.
(24) M. R. Pokhrel , K. Janik, S. H. Bossmann. Photoinitiated Synthesis and Characterization of P(MMA/DPB) Polymer Nanoparticles Using Poly(*N*-isopropylacrylamide) in Aqueous Solutions as a Template. *Macromolecules*, **2000**, 33 (10), 3577–3584.
(25) R. H. Fang, S. Aryal, C. M. Jack Hu, and L. Zhang**.** Quick Synthesis of Lipid-Polymer Hybrid Nanoparticles with Low Polydispersity Using a Single-Step Sonication Method. *Langmuir*. **2010**, 26(22), 16958–16962.
(26) J. Wu, X. Q. Liu, Y. C. Wang, J. Wang. Template-free synthesis of biodegradable nanogels with tunable sizes as potential carriers for drug delivery. *J. Mater. Chem.* **2009**, 19, 7856–7863.
(27) W. Wu, M. Aiello, T. Zhou, A. Berliner, P. Banerjee, S. Zhou. In-situ immobilization of quantum dots in polysaccharide-based nanogels for integration of optical pH-sensing, tumor cell imaging, and drug delivery. *Biomaterials*. **2010,** 31, 3023–3031.
(28) Y. Wang, S. Gao, W. H. Ye, H. S. Yoon, Y.Y. Yang. Co-delivery of drugs and DNA from cationic core–shell nanoparticles self-assembled from a biodegradable copolymer. *Nature Materials*, **2006,** 5, 791-96.

(29) R. T. Chacko, J. Ventura, J. Zhuang, S. Thayumanavan. Polymer nanogels: A versatile nanoscopic drug delivery platform. *Advanced Drug Delivery Reviews.* **2012,** 64, 836–851.
(30) Y. Qiu, K. Park. Environment-sensitive hydrogels for drug delivery. *Advanced Drug Delivery Reviews.* **2012,** 64, 49–60.
(31) E. O. Akala, P. Kopečková, J. Kopeček. Novel pH-sensitive hydrogels with adjustable swelling kinetics. *Biomaterials.* **1998**, 19(11-12), 1037-47.
(32) P. A. Vivero, E. F. Gabriel, C. A. Lorenzo, A. Concheiro. Improving the loading and release of NSAIDs from pHEMA hydrogels by copolymerization with functionalized monomers. *Journal of Pharmaceutical Sciences*, **2007**, 96 (4), 802–813.
(33) P. Chivukula, K. Dušek, D. Wang, M. D. Smrčková, P. Kopečková, J. Kopeček. Synthesis and characterization of novel aromatic azo bond-containing pH-sensitive and hydrolytically cleavable IPN hydrogels. *Biomaterials.* **2006**, 27(7) 1140–1151.
(34) Z. Amoozgar, L. Wang, T. Brandstoetter, S. S. Wallis, E. M. Wilson, M. S. Goldberg. Dual-layer surface coating of PLGA-based nanoparticles provides slow-release drug delivery to achieve metronomic therapy in a paclitaxel-resistant murine ovarian cancer model. *Biomacromolecules.* **2014**, 15(11), 4187-94.
(35) R. Duncan, R. Gaspar. Nanomedicine(s) under the Microscope. *Mol. Pharmaceutics*. **2011**, 8(6), 2101–2141.
(36) W. C. W. Chan, Bio-Applications of Nanoparticles. **2007**, *Springer*.
(37) S. D. Brown, P. Nativo, J. A. Smith, D. Stirling, P. R. Edwards, B. Venugopal, D. J. Flint, J. A. Plumb, D. Graham, N. J. Wheate. Gold Nanoparticles for the Improved Anticancer Drug Delivery of the Active Component of Oxaliplatin. *J. Am. Chem. Soc.* **2010**, 132 (13), 4678–4684.
(38) D. R. Bhumkar, H. M. Joshi, M. Sastry, V. B. Pokharkar. Chitosan Reduced Gold Nanoparticles as Novel Carriers for Transmucosal Delivery of Insulin. *Pharm. Res.* **2007**, 24(8), 1415-26.
(39) J. D. Rocca, D. Liu, W. Lin. Nanoscale Metal–Organic Frameworks for Biomedical Imaging and Drug Delivery. *Acc. Chem. Res.* **2011**, 44 (10), 957–968
(40) C. He, K. Lu, D. Liu, W. Lin. Nanoscale Metal−Organic Frameworks for the Co-Delivery of Cisplatin and Pooled siRNAs to Enhance Therapeutic Efficacy in Drug-Resistant Ovarian Cancer Cells. *J. Am. Chem. Soc.* **2014**, 136, 5181−5184.
(41) L. L. Tan, H. Li, Y. C. Qiu, D. X. Chen, X. Wang, R. Y. Pan, Y. Wang, S. X. A. Zhang, B. Wang, Y. W. Yang. Stimuli-responsive metal–organic frameworks gated by pillar[5]arene supramolecular switches. *Chem. Sci*. **2015**, 6**,** 1640-1644.
(42) P. Horcajada, T. Chalati, C. Serre, B. Gillet, C. Sebrie, T. Baati, J. F. Eubank, D. Heurtaux, P. Clayette, C. Kreuz, J. S. Chang, Y. K. Hwang, V. Marsaud, P. N. Bories, L. Cynober, S. Gil, G. Férey, P. Couvreur, R. Gref. Porous metal–organic-framework nanoscale carriers as a potential platform for drug delivery and imaging. *Nature Materials*. **2010**, 9, 172–178.
(43) H. A. Jeng, J. Swanson. Toxicity of metal oxide nanoparticles in mammalian cells. *J. Environ. Sci. Health A Tox. Hazard Subst. Environ. Eng.* **2006**, 41(12), 2699-711.
(44) N. Larson, H. Ghandehari. Polymeric Conjugates for Drug Delivery. *Chem. Mater.* **2012**, 24, 840−853.
(45) P. Bailon, A. Palleroni, C. A. Schaffer, C. L. Spence, W. J. Fung, J. E. Porter, G. K. Ehrlich, W. Pan, Z. X. Xu, M. W. Modi, A. Farid, W. Berthold, M. Graves. Rational

design of a potent, long lasting form of interferon: a 40kDa branched poly-ethylene glycol-conjugated interferon alpha-2a for the treatment of hepatitis C. *Bioconjug. Chem.* **2001**, 12, 195–202.
(46) V. Gaberc-Porekar, I. Zore, B. Podobnik, V. Menart. Obstacles and pitfalls in the PEGylation of therapeutic proteins. *Current Opinion in Drug Discovery & Development.* **2008**, 11(2), 242-250.
(47) A. D. Wong, M. A. DeWit, E. R. Gillies. Amplified release through the stimulus triggered degradation of self-immolative oligomers, dendrimers, and linear polymers. *Advanced Drug Delivery Reviews*. **2012**, 64(11), 1031–1045.
(48) C. Kelly, C. Jefferies, S. A. Cryan. Targeted Liposomal Drug Delivery to Monocytes and Macrophages. *Journal of Drug Delivery.* **2011,** 2011.
(49) M. J. Lawrence, G. D. Rees. Microemulsion-based media as novel drug delivery systems. *Advanced Drug Delivery Reviews*. **2000**, 45(1), 89–121.
(50) G. T. Vladisavljević, A. Laouini, C. Charcosset, H. Fessi, H. C.H. Bandulasena, R. G. Holdich. Production of liposomes using microengineered membrane and co-flow microfluidic device. *Colloids and Surfaces A: Physicochem. Eng. Aspects.* **2014**, 458, 168–177.
(51) M. Goldberg, R. Langer, X. Jia. Nanostructured materials for applications in drug delivery and tissue engineering. **2007.** *J. Biomater. Sci. Polymer Edn*, 18(3), 241–268.
(52) J. K. Oh, R. Drumright, D. J. Siegwart, K. Matyjaszewski. The development of microgels/nanogels for drug delivery applications. *Prog. Polym. Sci.* **2008**, 33, 448–477.
(53) P. A. Vivero, E. F. Gabriel, C. A. Lorenzo, A. Concheiro. Improving the loading and release of NSAIDs from pHEMA hydrogels by copolymerization with functionalized monomers. *Journal of Pharmaceutical Sciences*, **2007**, 96(4), 802–813.
(54) W. Lohcharoenkal, L. Wang, Y. C. Chen, Y. Rojanasaku. Protein Nanoparticles as Drug Delivery Carriers for Cancer Therapy. *BioMed Research International*. **2014,** 2014.
(55) A. O. Elzoghby, W. M. Samy, N. A. Elgindy. Protein-based nanocarriers as promising drug and gene delivery systems. *Journal of Controlled Release.* **2012**, 161(1), 38–49.
(56) S. Ko, S. Gunasekaran. Preparation of sub-100-nm β-lactoglobulin (βLG) nanoparticles. *J. Microencapsul.* **2006,** 23, 887–898.
(57) H. Urakami, J. Hentschel, K. Seetho, H. Zeng, K. Chawla, and Z. Guan. Surfactant-Free Synthesis of Biodegradable, Biocompatible, and Stimuli-Responsive Cationic Nanogel Particles. *Biomacromolecules* **2013**, 14, 3682−3688.
(58) C. Pérez, I. J. Castellanos, H. R. Costantino, W. A. Azzam, K. Griebenow. Recent trends in stabilizing protein structure upon encapsulation and release from bioerodible polymers. *J Pharm Pharmacol*. **2002**, 54(3), 301-13.
(59) T.R. Hoare, D. S. Kohane. Hydrogels in Drug Delivery: Progress and challenges. *Polymer*, **2008**, 49, 1993-2007.
(60) N. A. Peppas, J. Z. Hilt, A. Khademhosseini, R. Langer. Hydrogels in Biology and Medicine: From Molecular Principles to Bionanotechnology. *Adv. Mater.* **2006**, 18, 1345–1360.

(61) P. Edman, B. Ekman, I. Sjöholm. Immobilization of Proteins in Microspheres of Biodegradable Polyacryldextran. *Journal of Pharmaceutical Sciences.* **1980**, 69(7), 838–842.
(62) K. Raemdonck, B. Naeye, K. Buyens, R. E. Vandenbroucke, A. Høgset, J. Demeester, S. C. De Smedt. Biodegradable Dextran Nanogels for RNA Interference: Focusing on Endosomal Escape and Intracellular siRNA Delivery. *Adv. Funct. Mater.* **2009**, 19, 1406–1415.
(63) D. A. Heller, Y. Levi, J. M. Pelet, J. C. Doloff, J. Wallas, G. W. Pratt, S. Jiang , G. Sahay, A. Schroeder, J. E. Schroeder, Y. Chyan, C. Zurenko, W. Querbes, M. Manzano, D. S. Kohane, R. Langer, D. G. Anderson. Modular 'click-in-emulsion' bone-targeted nanogels. *Adv Mater.* **2012**, 25, 1449–1454.
(64) Y. Jiang, J. Chen, C. Deng, E. J. Suuronen, Z. Zhong. Click hydrogels, microgels and nanogels: Emerging platforms for drug delivery and tissue engineering. *Biomaterials.* **2014**, 35(18), 4969–4985.
(65) S. Kiese, A. Pappenberger, W. Friess, H. C. Mahler. Shaken, Not Stirred: Mechanical Stress Testing of An IgG1 Antibody. *J. Pharma. Sci.* **2008**, 97(10), 4347-4366.
(66) S. Papadimitriou, S. Dimitris, S. Achilias, D. N. Bikiaris. Chitosan-g-PEG Nanoparticles Ionically Crosslinked with Poly(glutamic acid) and Tripolyphosphate as Protein Delivery Systems. *International Journal of Pharmaceutics***, 2012**, 430, 318–327.
(67) S. K. H. Gulrez, S. Al-Assaf, G. O. Phillips. *Hydrogels: Methods of Preparation, Characterisation and Applications.* Progress in Molecular and Environmental Bioengineering – From Analysis and Modeling to Technology Applications. In: Angelo Carpi, editor. Rijeka: In Tech, 2011.
(68) L. S. M. Teixeira, J. Feijen, C. A. van Blitterswijk, P. J. Dijkstra, M. Karperien. Enzyme-catalyzed crosslinkable hydrogels: Emerging strategies for tissue engineering. *Biomaterials.* **2012**, 33, 1281-1290.
(69) F. Song, L. M. Zhang, J. F. Shi, N. N. Li. Novel casein hydrogels: Formation, structure and controlled drug release. *Colloids and Surfaces B: Biointerfaces*. **2010**, 79(1), 142–148.
(70) S. Toledano, R. J. Williams, V. Jayawarna, R. V. Ulijn. Enzyme-Triggered Self-Assembly of Peptide Hydrogels via Reversed Hydrolysis. *J. Am. Chem. Soc*. **2006**, 128, 1070-1071.
(71) M. Ehrbar, S. C. Rizzi, R. G. Schoenmakers, B. San Miguel, J. A. Hubbell, F. E. Weber, M. P. Lutolf. Biomolecular Hydrogels Formed and Degraded via Site-Specific Enzymatic Reactions. *Biomacromolecules*, **2007**, 8(10), 3000–3007.
(72) A. Kumari, S. K. Yadav, S. C. Yadav. Biodegradable polymeric nanoparticles based drug delivery systems. *Colloids and Surfaces B: Biointerfaces*. **2010**, 75(1), 1–18.
(73) T. Andersen, B. L. Strand, K. Formo, E. Alsberg, B. E. Christensen. Alginates as biomaterials in tissue engineering. *Carbohydr. Chem*. **2012**, 37, 227—258.
(74) J. Zhu, R. E. Marchant. Design properties of hydrogel tissue-engineering scaffolds. *Expert Rev. Med. Devices*. **2011,** 8(5), 607–626.
(75) M. Hamidi, A. Azadi, P. Rafiei. Hydrogel nanoparticles in drug delivery. *Advanced Drug Delivery Reviews.* **2008**, 60, 1638–1649.
(76) O. Wichterle, D. Lím. Hydrophilic gels for biological use. *Nature*, **1960**, 185, 117–118.

(77) J. Nesamony, P. R. Singh, S. E. Nada, Z. A. Shah, W. M. Kolling. Calcium Alginate Nanoparticles Synthesized Through a Novel Interfacial Cross-Linking Method as a Potential Protein Drug Delivery System. *Journal of Pharmaceutical Sciences*. **2012**, 101(6), 2177–2184.
(78) J. P. Rolland, B. W. Maynor, L. E. Euliss, A. E. Exner, G. M. Denison, J. M. DeSimone. Direct fabrication and harvesting of monodisperse, shape-specific nanobiomaterials. *J. Am. Chem. Soc.* **2005,** 127, 10096–100.
(79) A. Garcia, P. Mack, S. Williams, C. Fromen, T. Shen, J. Tully, J. Pillai, P. Kuehl, M. Napier, J. M. DeSimone, B. W. Maynor. Microfabricated Engineered Particle Systems for Respiratory Drug Delivery and Other Pharmaceutical Applications. *Journal of Drug Delivery.* **2012** (2012) Epub.
(80) E. Melgar, D. A. Goldthwait. Deoxyribonucleic Acid Nucleases. II. The Effects of Metals on the Metals on the Mechanism of Action of Deoxyribonulease I. *The Journal of Biological Chemistry*. **1968**, 243(17), 4409-4410.
(81) K. T. Nguyen, J. L. West. Photopolymerizable hydrogels for tissue engineering applications. *Biomaterials*. **2002**, 23(22), 4307–4314.
(82) J. J. Kasianowicz, E. Brandin, D. Branton, D. Deamer. W. *Proc. Nat. Acad. Sci.* **1996**, 93, 13770-13773.
(83) Y. Hu, J. Wang, H. Wang, Q. Wang, J. Zhu, Y. Yang. Microfluidic Fabrication and Thermoreversible Response of Core/Shell Photonic Crystalline Microspheres Based on Deformable Nanogels. *Langmuir*, **2012**, 28, 17186−17192.
(84) L. C. Deaño, F. J. G. Rosales, F. T. Pinho, M. A. Alves, M. S. N. Oliveira. Nanogel formation of polymer solutions flowing through porous media. *Soft Matter*, **2012**, 8, 6445-6453.
(85) J. J. Water, Y. T. Kim, M. J. Maltesen, H. Franzyk, C. Foged, H. M. Nielsen. Hyaluronic Acid-Based Nanogels Produced by Microfluidics-Facilitated Self-Assembly Improves the Safety Profile of the Cationic Host Defense Peptide Novicidin. *Pharm. Res.* **2015,** DOI**:** 10.1007/s11095.
(86) H. Zhang, E. Tumarkin, R. M. A. Sullan, G. C. Walker, E. Kumacheva. Exploring Microfluidic Routes to Microgels of Biological Polymers. *Macromol. Rapid Commun*. **2007**, 28, 527–538.
(87) C. X. Zhao, L. He, S. Z. Qiao, A. P. J. Middelberg. Nanoparticle synthesis in microreactors. *Chemical Engineering Science*. **2011**, 66(7), 1463–1479.
(88) N. Reddy, Z. Shi, H. Xu, Y. Yang. Development of wheat glutenin nanoparticles and their biodistribution in mice. *J. Biomed. Mater. Res. A*. **2015**, 103(5), 1653-8.
(89) K. H. Bae, H. Mok, T. G. Park. Synthesis, characterization, and intracellular delivery of reducible heparin nanogels for apoptotic cell death. *Biomaterials*. **2008**, 23, 3376-83.
(90) D. Muraoka, N. Harada, T. Hayashi, Y. Tahara, F. Momose, S. Sawada, S. A. Mukai , K. Akiyoshi, H. Shiku. Nanogel-based immunologically stealth vaccine targets macrophages in the medulla of lymph node and induces potent antitumor immunity. *ACS Nano.* **2014**, 8(9), 9209-18.
(91) I. Gülseren, Y. Fang, M. Corredig. Zinc incorporation capacity of whey protein nanoparticles prepared with desolvation with ethanol. *Food Chem*. **2012,** 135(2), 770-774.

(92) R. P. Narayanan , G. Melman, N. J. Letourneau, N. L. Mendelson, A. Melman. Photodegradable Iron(III) Cross-Linked Alginate Gels. *Biomacromolecules*, **2012**, 13(8), 2465–2471.
(93) V. Bocharova, O. Zavalov, K. MacVittie, M. A. Arugula, N. V. Guz, M. E. Dokukin, J. Halámek, I. Sokolov, V. Privman, E. Katz. A biochemical logic approach to biomarker-activated drug release. *J. Mater. Chem*., **2012**, 22, 19709–19717.
(94) Z. Jin, A. M. Harvey, S. Mailloux, J. Halámek, V. Bocharova, M. R. Twiss, E. Katz. Electrochemically stimulated release of lysozyme from an alginate matrix cross-linked with iron cations. *J. Mater. Chem*., **2012**, 22, 19523–19528.
(95) D. Puri. *Textbook of Medical Biochemistry*. 2nd ed.; New Delhi: Elsevier, 2006.
(96) H. H. Perkampus, H. C. Grinter, T. L. Threlfall. *UV-Vis Spectroscopy and its Applications.* 1992. Berlin: Springer-Verlag.
(97) B. J. Berne, R. Pecora. *Dynamic Light Scattering with Applications to Chemistry, Biology, and Physics.* 2nd ed.; New York: Wiley, 1976.
(98) W. Schärtl. *Light Scattering from Polymer Solutions and Nanoparticle Dispersions.* 1st ed.; Heidelberg: Springer, 2010.
(99) Y. Wang, P. J. Griffin, A. Holt, F. Fan, A. P. Sokolov. Observation of the slow, Debye-like relaxation in hydrogen-bonded liquids by dynamic light scattering. *The Journal of Chemical Physics.* **2014**, 140, 104(10).
(100) F. Mallamace, C. Corsaro, N. Leone, V. Villari, N. Micali, S. H. Chen. On the ergodicity of supercooled molecular glass-forming liquids at the dynamical arrest: the o-terphenyl case. *Sci Rep.* **2014**, 17(4), 3747.
(101) S. Vahabi, B. N. Salman, A. Javanmard. Atomic Force Microscopy Application in Biological Research: A Review Study. *Iran J Med Sci.* **2013**, 38(2), 76–83.
(102) G. Teobaldi, K. Lämmle, T. Trevethan, M. Watkins, A. Schwarz, R. Wiesendanger, A. L. Shluger. Chemical Resolution at Ionic Crystal Surfaces Using Dynamic Atomic Force Microscopy with Metallic Tips. *Phys. Rev. Lett.* **2011**, 106(21), Epub.
(103) P. Eaton, P. West. *Atomic force Microscopy*. Oxford: Oxford University Press, 2010.
(104) J. S. Higgins, H. Benoît. *Polymers and neutron scattering*. Oxford: Clarendon press, 1994.
(105) W. T. Heller, V. S. Urban, G. W. Lynn, K. L. Weiss, H. M. O'Neill, S. V. Pingali, S. Qian, K. C. Littrell, Y. B. Melnichenko, M. V. Buchanan, D. L. Selby, G. D. Wignall, P. D. Butler, D. A. Myles. The Bio-SANS instrument at the High Flux Isotope Reactor of Oak Ridge National Laboratory. *J. Appl. Cryst.* **2014,** 47, 1238-1246.
(106) S. M. King. Small-angle neutron scattering. In *Modern Techniques for Polymer Characterisation.* Pethrick, R. A., Dawkins, J. V., Eds. New York: Wiley, 1999.
(107) B. Hammouda. *The SANS Toolbox*. **2008**, Gaithesburg, MD: Center for Neutron Research, National Institute of Standards and Technology, 657.
(108) A. J. Jackson. *Introduction to Small-Angle Neutron Scattering and Neutron Reflectometry.* 2008. NIST.
(109) B. Hammouda. Analysis of the Beaucage model. *J. Appl. Crystallogr.* **2010,** 43, 1474–1478.
(110) G. Beaucage. *Polymer Science: A Comprehensive Reference.* K. Matyjaszewski, M. Möller. Eds. Oxford: Elseivier, 2012.
(111) G. Beaucage. Approximations Leading to a Unified Exponential/Power-Law Approach to Small-Angle Scattering. *J. Appl. Cryst.* **1995,** 28, 717-728.

(112) G. D. Wignall, K. C. Littrell, W. T. Heller, Y. B. Melnichenko, K. M. Bailey, G. W. Lynn, D. A. Myles, V. S. Urban, M. V. Buchanan, D. L. Selby, P. D. J. Butler. The 40 m general purpose small-angle neutron scattering instrument at Oak Ridge National Laboratory. *Appl. Crystallogr.* **2012**, 45(5), 990–998.
(113) S. Holder. *Viscosimetry of Polymers and Polyelectrolytes*. Werner-Michael Kulicke, Christian Clasen. Eds. Hamburg: Springer-Verlag, 2004.
(114) P. A. Janmey, M. Schliwa. Rheology. *Current Biology*. **2008**, 18(15), R639–R641
(115) Nhan Phan-Thien. *Understanding viscoelasticity: an introduction to Rheology*. 2nd ed. Springer. 2013.
(116) T. G. Mezger. *The Rheology Handbook: For Users of Rotational and Oscillatory Rheometers.* 2nd ed. Hannover: Vincentz Network, 2006.
(117) K. P. Menard. *Dynamic Mechanical Analysis: A Practical Introduction*. Boca Raton: CRC Press LLC, 1999.
(118) I. M. N. Vold, K. A. Kristiansen, B. E. Christensen. A Study of the Chain Stiffness and Extension of Alginates, in Vitro Epimerized Alginates, and Periodate-Oxidized Alginates Using Size-Exclusion Chromatography Combined with Light Scattering and Viscosity Detectors. *Biomacromolecules*. **2006**, 7, 2136-2146.
(119) A. A. Schilt. *Analytical applications of 1,10-phenanthroline and related compounds.* Oxford, UK: Pergamon Press, 1969.
(120) C. Roy, T. Budtova, P. Navard. Rheological Properties and Gelation of Aqueous Cellulose-NaOH Solutions. *Biomacromolecules*. **2003**, 4, *259-264.*
(121) P. C. Hiemenz, T. P. Lodge. *Polymer Chemistry*. 2nd Ed. Boca Raton: CRC Press. 2007.
(122) B. Bhushan. *Scanning Probe Microscopy in Nanoscience and Nanotechnology*, 3; Springer Science & Business Media: New York, 2012.
(123) A. Shkilnyy, A. Friedrich, B. Tiersch, S. Schöne, M. Fechner, J. Koetz, C. W. Schläpfer, A. Taubert. Poly(ethylene imine)-Controlled Calcium Phosphate Mineralization. **2008**, *Langmuir*, 24(5), 2102–2109.
(124) M. A. Lawn, R. V. Goreham, J. Herrmann, Å. K. Jämting. Particle number density gradient samples for nanoparticle metrology with atomic force microscopy. *J. Micro/Nanolith. MEMS MOEMS*. **2012**, 11(1), Epub.
(125) O. Zavalov, V. Bocharova, V. Privman, E. Katz. Enzyme-Based Logic: OR Gate with Double-Sigmoid Filter Response. *J. Phys. Chem. B*, **2012**, 116 (32), pp 9683–9689.
(126) J. Ilavsky, P. R. Jemian. Irena: tool suite for modeling and analysis of small-angle scattering. *J. Appl. Cryst.* **2009**, 42, 347-353.
(127) K. Piontek, M. Antorini, T. J. Choinowski. *Biol. Chem.* **2002**, 277, 37663−37669.
(128) Y. Wu, Y. Jiang, J. Jiao, M. Liu, F. Hu, B. S. Griffiths, H. Li. Adsorption of Trametes versicolor laccase to soil iron and aluminum minerals: Enzyme activity, kinetics and stability studies. *Colloids and Surfaces B: Biointerfaces.* **2014**, 114, 342– 348.
(129) M. Ferrari, T. Desai, S. N. Bhatia. Eds. *BioMEMS and Biomedical Nanotechnology: Volume III*. Springer Science & Business Media: New York, 2007.
(130) C. Chassenieux, T. Nicolai, L. Benyahia. Rheology of associative polymer solutions. *Current Opinion in Colloid & Interface Science.* **2011**, 16(1), 18–26.
(131) M. A. da Silva, F. Bode, I. Grillo, C. A. Dreiss. Exploring the Kinetics of Gelation and Final Architecture of Enzymatically Cross-linked Chitosan/Gelatin Gels. *Biomacromolecules*. **2015**, 16, 1401-1409.

(132) C. Wu, C. Strehmel, K. Achazi, L. Chiappisi, J. Dernedde, M. C. Lensen, M. Gradzielski, M. B. A. Schumacher, R. Haag. Enzymatically Cross-Linked Hyperbranched Polyglycerol Hydrogels as Scaffolds for Living Cells. *Biomacromolecules.* **2014,** 15 (11), 3881-3890.

VITA

Danna Sharp was born in Knoxville Tennessee in April of 1989. She attended East Tennessee State University upon graduation of high school. After two years of study, she transferred to the University of Tennessee Knoxville and obtained her Bachelors of Science Degree in Biochemistry and Molecular Biology. During her 5 years of undergraduate study she obtained summer internships at various institutions including Oak Ridge National Laboratory, Pacific Northwest National Laboratory, University of Tennessee Knoxville, and Vanderbilt University. She then moved on to study polymer chemistry at UTK in Dr. Alexei Sokolov's research group. She will obtain her Master's degree working on polymer development for drug delivery.